ELECTRONIC AND STRUCTURAL STUDIES OF FREE AND SUPPORTED METAL CLUSTERS AND MOLECULES

BY
KARI RYTKÖNEN

Academic Dissertation
for the Degree of
Doctor of Philosophy

To be presented, by permission of the
Faculty of Mathematics and Natural Sciences
of the University of Jyväskylä,
for public examination in Auditorium FYS-1 of the
University of Jyväskylä on October 20, 2006
at 12 o'clock noon

Jyväskylä, Finland
October 2006

Preface

This work has been carried out at the Department of Physics and at the Nanoscience Center of the University of Jyväskylä during the years 2000-2006.

I would like to thank my supervisor docent Jaakko Akola for his remarkable efforts with my studies. I would also like to thank professor Matti Manninen, and the whole Department of Physics for providing a welcoming setting for my studies.

My sincerest compliments to Kimmo Kärkkäinen who helped me with technical problems and encouraged me when I had doubts, and to Kirsi Manninen, Pekka Koskinen, and many other co-students with whom I had honour to study and spend spare time.

Finally I want to express my gratitude to my parents and siblings for all the support, and my warmest thanks to my friends Marko Ikonen, Jarmo Seppänen, and Suvi Nieminen who reminded me that there is life outside work.

Jyväskylä, October 2006

Kari Rytkönen

Abstract

Metal clusters have attracted a growing attention during the past three decades. This interest is caused by the uniquely different properties of these finite systems in comparison to the corresponding bulk matter. The metallic evolution as a function of the cluster size, and the intriguing interaction of alkali metals with highly oriented pyrolytic graphite (HOPG) surface are among the most widely studied topics within the cluster physics. Carbon nanotubes, on the other hand, are very promising building blocks for nanoelectronics and chemical sensors.

In this thesis, we employ the density functional theory to examine the electronic properties and structures of small magnesium clusters, alkali metals on a graphite surface and carbon nanotubes which are functionalized with cyclic macromolecules.

The slow non-monotonic metallic evolution of magnesium clusters up to cluster size Mg_{13} was verified with "magic" cluster sizes of four and ten atoms that were particularly stable because of their closed electron shells. The widely debated interaction of alkali metals with HOPG was found to be ionic, and the experimentally found overlayer constructions and the related physical and chemical properties of alkali metal adatoms as well as the anomalous behavior of sodium were studied. The modification of electronic properties of (4,4), (8,0), and (4,0) single-walled carbon nanotubes with cyclic crown ether and cyclodextrin macromolecules were studied by threading them on carbon nanotubes. It was found that this kind of polyrotaxane complexes have essentially the same electronic properties as pristine nanotubes unless chemical cross-linkage between the tube and the macromolecule is enforced. However, it was found that it is possible to tune the conductivity of carbon nanotubes with chemical cross-linking.

List of Publications

I J. Akola, K. Rytkönen, and M. Manninen, *Metallic evolution of small magnesium clusters*, Eur. Phys. J. D **16**, 21-24 (2001).

II K. Rytkönen, J. Akola, and M. Manninen, *Sodium atoms and clusters on graphite by density functional theory*, Phys. Rev. B **69**, 205404 (2004).

III J. Akola, K. Rytkönen, and M. Manninen, *Electronic Properties of Single-Walled Carbon Nanotubes inside Cyclic Supermolecules*, J. Phys. Chem. B **110**, 5186 (2006).

IV K. Rytkönen, J. Akola, and M. Manninen, *Density functional study of alkali atoms and monolayers on graphite (0001)*, Phys. Rev. B, submitted.

The author has performed main part of the numerical work in all the publications, written drafts of the publications II and IV, and participated in writing the publications I and III.

Contents

1 Introduction

1.1 Atomic Clusters

An atomic cluster is an object that comprises from few up to hundreds of thousands of atoms of one or more elements. Even if the class of clusters is defined with the strictest manner it still includes a vast amount of objects, and even more if carbon nanotubes and macromolecules are counted. Cluster research is a moderately new field of physics which has been growing explosively during the last few decades. Despite this applications of metal clusters have been around for hundreds of years as, for example, glass coloured with metal particles was produced for the flamboyant window scenes of churches.

Until the early 1980's there was two different views on the cluster behavior: One was that the properties of clusters can be predicted from the properties of single particles and bulk matter by scaling, and the other was that clusters behave like molecules, and that there is no relation between different cluster sizes and clusters with different elements, so that every cluster is essentially unique. This was changed in 1984 as Knight *et al.* produced and detected clusters of alkali metals with up to 100 atoms [1, 2]. Their results revealed size-dependent behavior, where the electronic structure of clusters appeared to reflect that of a spherical potential well: Clusters in which the number of valence electrons matched to the spherical shell-closing numbers were
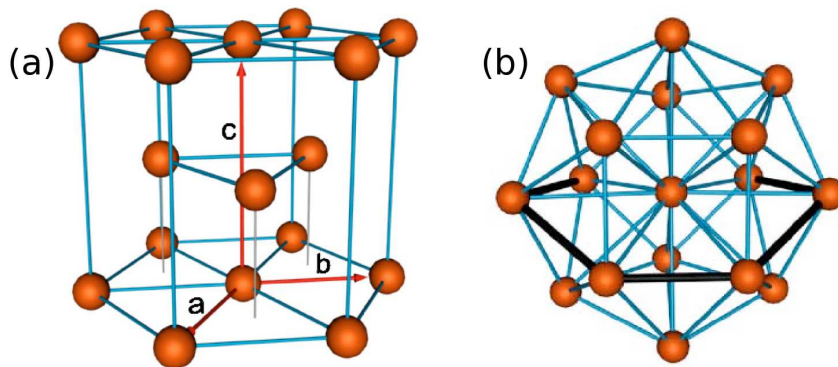
Figure 1.1: The atomic coordination in clusters differs usually from that in bulk: (a) The bulk hcp lattice of Mg, and (b) the geometry of Mg_{20} [5].
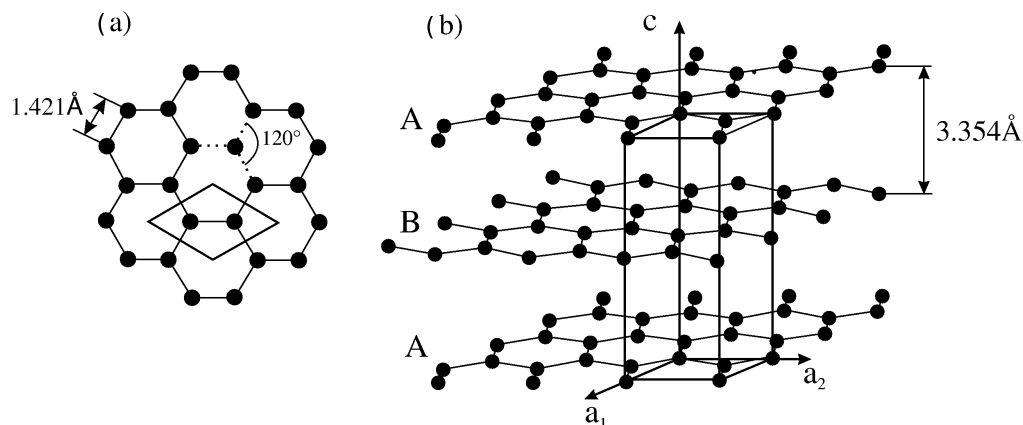
Figure 1.2: (a) The structure of a graphene layer, and (b) three-dimensional graphite [6].

more abundant in the spectrum. Ekardt predicted this behavior theoretically virtually simultaneously [3, 4].

Typical metallic features such as a good heat and electronic conductance, formability, light reflectivity, and delocalization of electrons (metallic bond) are bulk properties that do not necessarily apply to zero-dimensional metal atoms or small clusters. Thereby, these objects do not have a band structure. Another crucial difference between clusters and bulk material is that a large portion of the cluster atoms, sometimes all of them, can be considered as surface atoms (see Fig. 1.1). Consequently, the atoms in clusters have fewer nearest-neighbor atoms, and they are exposed to their surroundings. At which size the metallic properties emerge, and what are the properties of small "sub-metallic" pieces of metal need to be studied in order to achieve a fundamental understanding of materials. This is especially important because applications based on metal clusters, such as functionalized materials, nanodevices and electric nanocircuits have been proposed, and to some extend already developed.

1.2   Role of Surface In Cluster Research

Surface science is a wide research area which involves physicists, chemists and biologists. It has its roots in solid state and molecular physics, physical and inorganic chemistry, catalysis, microelectronics, thin film technologies, electrochemistry and various other research subjects. Processes at solid surfaces can affect industrial processes both profitably (e.g. catalysis) and harmfully (e.g. corrosion). Chemical reactions at two-dimensional solid surfaces can differ remarkably from those in three-dimensions, and reaction pathways with lower activation energies can exist.

In order to build planar nanostructures, for example electric circuits, some kind of a substrate is usually needed. Similarly, studying the physical and chemical properties of clusters is often easier when they are attached on a substrate. Clusters and nanostructures interact with the substrate, and their geometries and properties can change. The cluster-substrate interaction can lead to novel materials and new useful applications, but it can cause problems if the original features of the cluster or constructed nanostructure should be maintained. Therefore, to make controlled experiments a suitable substrate material has to be chosen. The planar, chemically inert, and layered structure of highly oriented pyrolytic graphite (HOPG, see Fig. 1.2) is in many cases a potential candidate, because one can split smooth and durable surfaces from it that can be cleaned easily and used as a weakly interacting (inert) substrate.

A vast number of studies has been performed on alkali metals on graphite surface (see review [6] and the references therein). Alkali metals are called simple metals, because they have only one valence electron, and their behavior can be predicted in many respects from a simple "jellium" model. The interaction with graphite is much more complicated, though, and alkali metal adatoms prefer a different binding site (hollow site) on the surface than hydrogen (above a carbon atom), which also has one valence electron [7]. In fact, it is still under debate whether the binding between alkali metals and graphite is of ionic, metallic, or covalent type. So far, most studies have concentrated on potassium, but reports on other alkali metals have emerged recently. However, there is still place for research as there are discrepancies between experimental and theoretical results, and even between different theoretical approaches [6]. This is due to the different approximations that have to be incorporated in order to simulate many-particle system consisting of a nanoscale object (cluster) sitting on a macroscopic substrate.

1.3   Carbon Nanotubes, Crown Ethers, Cyclodextrins, and Their Complexes

Carbon nanotubes (CNTs) are one-dimensional, hollow, and tubular structures which are formed via self-assembly under certain conditions, although the mechanism itself is not yet fully understood [8, 9]. The CNT walls can be described as graphene-like hexagonal carbon networks, and there are single-walled carbon nanotubes (SWNT) and multi-walled carbon nanotubes (MWNT). Experimentally, CNTs were observed already by Morinobu Endo in 1970's [10], but it was only after the finding of fullerenes by Kroto and Smalley (in 1985) [11], though, that Smalley speculated about the existence of carbon nanotubes of dimensions comparable to C_{60}. After Smalley's speculation Iijima reported in 1991 about his experimental observation of carbon nanotubes using a transmission electron microscope [12].
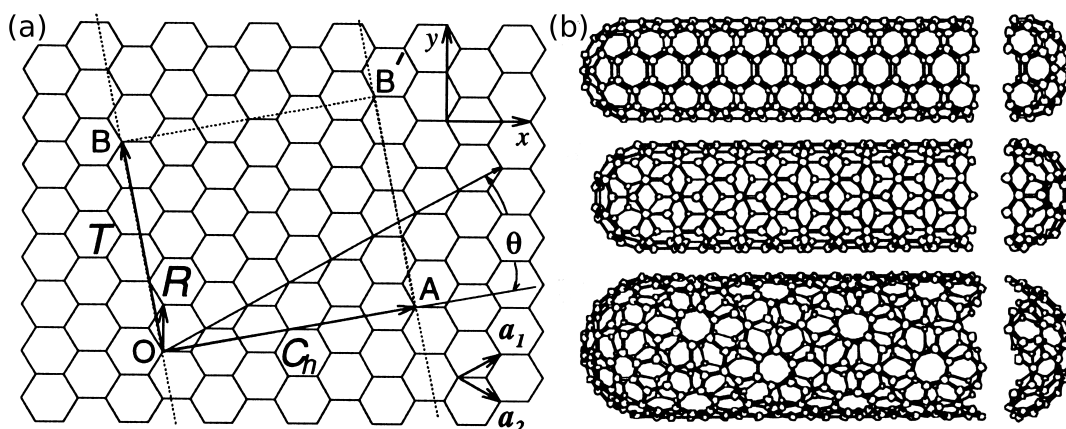
Figure 1.3: (a) The unrolled honeycomb lattice of carbon nanotube [13]. If O and A, as well as B and B' are connected, a chiral (4,2) carbon nanotube is obtained. Chirality is defined by a vector $C_h = \vec{OA} = (4,2)$, and T stands for a translation vector ($T = \vec{OB} = (4,-5)$). (b) Picture of three types of carbon nanotubes [13]: an "armchair" (n,n) nanotube, a "zigzag" (n,0) nanotube and a "chiral" (n,m) nanotube (intermediate of the two former structures).

The CNT type is defined by the orientation of the hexagonal network in relation to the tube axis (chirality, see Fig. 1.3). Carbon nanotubes have fascinating properties, such as an exceptional mechanical strength and electronic conductance, and CNTs are either conductors, semiconductors or insulators depending on the chirality [13]. They have inspired various possible applications, e.g. durable or electronically conducting fabrics have been manufactured already, and their potential usage in nanoelectronics is widely studied. Many of their fascinating properties can be explained by the graphene-like wall structure.

Crown ethers and cyclodextrins are other examples of self-assembled nanostructures that have applications in physics and chemistry [14, 15]. Both of them are circular macromolecules (macrocycles) with various radii. Macromolecules of the $(-CH_2CH_2O-)_n$ type ($n \geq 4$), i.e. consisting of four or more ethyleneoxy units, are generally referred to as crown ethers because of their crown-like appearance. Cyclodextrins resemble a truncated cone, and they consist of glucopyranoce rings (seven of them in β-cyclodextrin). These kind of circular molecules have inspired the construction of rotaxanes, where a linear molecule is threaded through a circular molecule, and the ring is locked by bulky stoppers at both ends of the linear molecule (see Fig. 1.4) [16]. Thereby, these two molecules are prevented from dethreading by physical obstacles while they do not have any chemical bonds between them. This kind of structures give promise of constructing, for example, molecular engines and chemical sensors. Rotaxanes with many circular molecules are called as polyrotaxanes, and rotaxanes without any bulky stoppers are called as pseudorotaxanes.
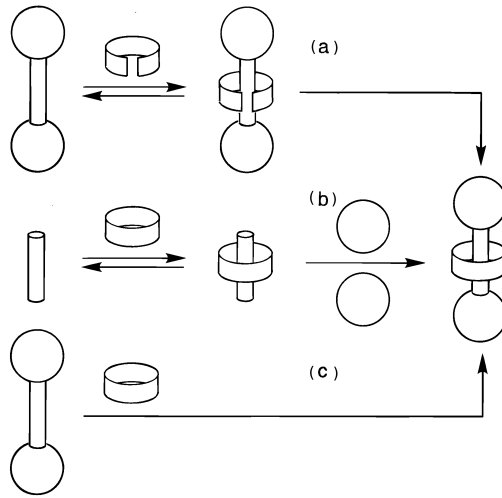
Figure 1.4: Three construction mechanisms of rotaxane: (a) "clipping", (b) "threading", (c) "slippage" [17].

The electronic and mechanical properties of CNTs can be modified with particle beams and chemically (functionalization). Furthermore, nanotubes can be adjusted so that they can be used as chemical sensors, or a one dimensional quantum dot network can be assembled by embedding ions inside them. One possible way to functionalize CNTs could be to use them in the role of the linear molecule in rotaxanes. Crown ethers and cyclodextrins could then be threaded on them, because they have both hydrophobic and hydrophilic parts and tend to attach onto organic macromolecules.

1.4   About This Thesis

In this thesis, we study the electronic structure of various optimized nanostructures by employing the Kohn-Sham (KS) formalism of the density functional theory (DFT) in conjunction with molecular dynamics and direct geometry optimization methods. This thesis consists of this introductory part and four publications. In Chapter 2, a theoretical background for the quantum mechanical many-body problem and molecular dynamics methods are presented. In Chapter 3, the density functional theory, and its applications are introduced. The evolution of metallization and its indicators are discussed in the case of small magnesium clusters in Section 4.1. The main part of this work concerns electronic structure calculations of alkali metal atoms on a graphite surface, and they are discussed extensively in Section 4.2. Final topic of pseudorotaxane complexes formed by threading circular macromolecules (crown ethers, β-cyclodextrin) on small SWNTs is discussed in Section 4.3.

2 Quantum Mechanical Many-Body Problem: Foundation and Simplifications

2.1 Time Independent Many-Body Schrödinger Equation

In principle, the electronic structure and properties of a quantum mechanical many-body system can be solved from the time-independent many-body Schrödinger equation

$$H\Psi = E\Psi, \tag{2.1}$$

where H is the Hamiltonian of the system, Ψ is the corresponding wave function and E is the total energy. For a system of N electrons and M nuclei in a zero external potential, the Hamiltonian is of the form (atomic units)

$$H = -\sum_{i=1}^{N} \frac{1}{2}\nabla_i^2 - \sum_{I=1}^{M} \frac{1}{2M_I}\nabla_I^2 - \sum_{i=1}^{N}\sum_{I=1}^{M} \frac{Z_I}{r_{iI}} + \sum_{i=1}^{N}\sum_{j>i}^{N} \frac{1}{r_{ij}} + \sum_{I=1}^{M}\sum_{J>I}^{M} \frac{Z_I Z_J}{R_{IJ}}, \tag{2.2}$$

where ∇_i^2 and ∇_I^2 are differential operators which operate with respect to the coordinates of electron i (r_i) and nucleus I (R_I), M_I is the ratio of the mass of nucleus I to the mass of an electron, Z_I and Z_J are atomic numbers of nuclei I and J, and r_{iI}, r_{ij} and R_{IJ} are the distances between electron i and nucleus I, electrons i and j, and nuclei I and J, respectively [18]. The first two terms in Eq. (2.2) are the kinetic operators of electrons and nuclei, and the last three terms are the Coulomb interaction between electrons and nuclei, electrons, and nuclei, respectively.

2.2 Born-Oppenheimer Approximation

Solving the many-body Schrödinger equation exactly is usually impossible, and simplifying approximations are needed. One of the most practical approximations is the so-called Born-Oppenheimer (BO) approximation [18], where the wave function Ψ of the whole system is separated into independent electron and nucleon parts Ψ_{elec} and Ψ_{nucl}, so that

$$\Psi = \Psi_{elec}\Psi_{nucl}. \tag{2.3}$$

This separation is justified as the mass of a nucleus is of the order of 10^3-10^5 larger compared to that of an electron. Therefore, nuclei move considerably slower than electrons, and they can be considered as fixed during the optimization of the electronic structure if the studied time interval is short enough. Consequently, the electronic and nuclear problem can be separated, and the electronic problem is described by the electronic Schrödinger equation

$$H_{elec}\Psi_{elec} = E_{elec}\Psi_{elec}, \tag{2.4}$$

where the electronic Hamiltonian is of the form

$$H_{elec} = -\sum_{i=1}^{N}\frac{1}{2}\nabla_i^2 - \sum_{i=1}^{N}\sum_{I=1}^{M}\frac{Z_I}{r_{iI}} + \sum_{i=1}^{N}\sum_{j>i}^{N}\frac{1}{r_{ij}}. \tag{2.5}$$

Solving Eq. (2.4) gives then the electronic state

$$\Psi_{elec} = \Psi_{elec}(\{\mathbf{r_i}\}; \{\mathbf{R_I}\}), \tag{2.6}$$

where the electronic coordinate r_i is a variable, and the nuclear coordinate R_I is a parameter.

After the electronic energy E_{elec} is known, the total ground state energy can be calculated by adding the nuclear Coulomb repulsion term to the electronic energy,

$$E_{tot} = E_{elec} + \sum_{I=1}^{M}\sum_{J>I}^{M}\frac{Z_I Z_J}{R_{IJ}}. \tag{2.7}$$

The electronic problem is now solved by solving the Eqs. (2.4) and Eq. (2.7).

The electronic energy

$$E_{elec} = \langle \Psi_{elec} | H_{elec} | \Psi_{elec} \rangle, \qquad (2.8)$$

has a parametric dependence on the nuclear coordinates,

$$E_{elec} = E_{elec}(\{\mathbf{R_I}\}). \qquad (2.9)$$

This gives rise to the useful Hellman-Feynman theorem [19, 20] in which the forces acting on nuclei are derived from the classical potential

$$V(\{\mathbf{r_i}\}; \{\mathbf{R_I}\}) = -\sum_{i=1}^{N}\sum_{I=1}^{M} \frac{Z_I}{r_{iI}} + \sum_{i=1}^{N}\sum_{j>i}^{N} \frac{1}{r_{ij}} + \sum_{I=1}^{M}\sum_{J>I}^{M} \frac{Z_I Z_J}{R_{IJ}}, \qquad (2.10)$$

which includes all the Coulombic interactions. By differentiating E_{elec} with respect to the components of ionic coordinates $R_{I,\alpha}$, where $\alpha = x, y, z$, we get the forces acting on nuclei

$$
\begin{aligned}
F_{I,\alpha} &= -\frac{\partial E_{elec}(\{\mathbf{R_I}\})}{\partial R_{I,\alpha}} = -\langle \Psi_{elec} | \frac{\partial H_{elec}}{\partial R_{I,\alpha}} | \Psi_{elec} \rangle \\
&= -\langle \Psi_{elec} | \frac{\partial V(\{\mathbf{r_i}\}; \{\mathbf{R_I}\})}{\partial R_{I,\alpha}} | \Psi_{elec} \rangle.
\end{aligned} \qquad (2.11)
$$

A more detailed derivation of this result is given in ref. [20].

2.3   Electronic Solution

Generally, if an electronic system is described by a state Ψ, the corresponding energy is

$$E[\Psi] = \frac{\langle \Psi | H | \Psi \rangle}{\langle \Psi | \Psi \rangle}, \qquad (2.12)$$

where Ψ does not have to be the ground-state wave function of the Schrödinger equation [21]. If the wavefunction is normalized ($\langle\Psi|\Psi\rangle = 1$), then the energy is simply the expectation value $E[\Psi] = \langle\Psi|H|\Psi\rangle$. Every state Ψ that satisfies the Schrödinger equation gives one of the eigenvalues of H, and therefore, if E_0 is the ground state energy of the system, we have

$$E[\Psi] \geq E_0. \tag{2.13}$$

Consequently, a full minimization of the functional $E[\Psi]$ with respect to all allowed N electron states gives the ground state energy E_0, and hence, the exact ground state Ψ_0. This is called as the variational method.

In practice, it is too difficult to perform the variational method exactly, and a trial wave function has to be constructed. Minimization is then performed by optimizing the parameters of this trial wave function. The form of the trial wave function determines how close to the real ground state energy one can get. Most often the many-body wave function is described in terms of separable single-particles. This is done by introducing a one-particle Schrödinger equation $h_i\psi_i = \varepsilon_i\psi_i$, where h_i is the one-particle Hamiltonian, ψ_i is the corresponding eigenfunction, and ε_i is the eigenenergy. This 'trick' can not be done without complications as the electron-electron interaction plays an important role in reality, and usually some kind of an effective potential has to be included.

Typical trial wave functions have the origin in the quantum mechanical Hartree, Hartree-Fock (HF) and Configuration Interaction (CI) methods [18].

In the Hartree method, the trial wave function is the so-called Hartree product (HP)

$$\Psi^{HP}(\mathbf{x}_1, \mathbf{x}_2, \ldots, \mathbf{x}_N) = \psi_i(\mathbf{x}_1)\psi_j(\mathbf{x}_2)\ldots\psi_k(\mathbf{x}_N), \tag{2.14}$$

where $\mathbf{x}_n$ (n=1,2,...,N) includes both the position and spin of the nth particle, and $\{\psi_m(\mathbf{x}_n)\}$ (m=i,j,...,k) are the non-interacting (orthonormal) single-particle spin orbitals. This product satisfies the above-mentioned single-particle Schrödinger equations. The problem with the Hartree product is that it does not fulfill the antisymmetry requirement that comes from the Pauli exclusion principle for fermions. In the Hartree-Fock (HF) theory, the normalized wave function is antisymmetrized by forming a Slater determinant

$$\begin{aligned}
\Psi^{HF}(\mathbf{x}_1, \mathbf{x}_2, \ldots, \mathbf{x}_N) &= \frac{1}{\sqrt{N!}} \begin{vmatrix} \psi_i(\mathbf{x}_1) & \psi_j(\mathbf{x}_1) & \ldots & \psi_k(\mathbf{x}_1) \\ \psi_i(\mathbf{x}_2) & \psi_j(\mathbf{x}_2) & \ldots & \psi_k(\mathbf{x}_2) \\ \vdots & \vdots & \ddots & \vdots \\ \psi_i(\mathbf{x}_N) & \psi_j(\mathbf{x}_N) & \ldots & \psi_k(\mathbf{x}_N) \end{vmatrix} \\
&=: \frac{1}{\sqrt{N!}} det[\psi_i, \psi_j, \ldots, \psi_k].
\end{aligned} \tag{2.15}$$

Using this trial wave function in the calculation of the electronic energy gives the so-called Hartree-Fock energy (E_{HF}), which differs from the real energy E. The difference between the real energy and the Hartree-Fock energy,

$$E_{corr}^{HF} = E - E_{HF}, \tag{2.16}$$

is called the correlation energy [18], and the determination of E_{corr}^{HF} is a major problem in the many-body theory [21]. The real energy can be calculated, in principle, by the CI method which uses an infinite sum of determinants

$$\Psi = c_0 |\Psi_0\rangle + \sum_{a,r} c_a^r |\Psi_a^r\rangle + \sum_{\substack{a<b \\ r<s}} c_{ab}^{rs} |\Psi_{ab}^{rs}\rangle + \sum_{\substack{a<b<c \\ r<s<t}} c_{abc}^{rst} |\Psi_{abc}^{rst}\rangle + \ldots, \tag{2.17}$$

where $|\Psi_0\rangle$ is the ground state of the Hartree-Fock determinant. In $|\Psi_a^r\rangle$ electron a is excited to the virtual state r, in $|\Psi_{ab}^{rs}\rangle$ electron a is excited to the virtual state r and electron b to the virtual state s, and so on. The corresponding coefficients related to these terms are c_0, c_a^r, c_{ab}^{rs}, and so on. In practice, only the most important terms are taken into consideration.

2.4 Born-Oppenheimer and Car-Parrinello Molecular Dynamics

In order to study the time evolution of an atomic or molecular system exactly, one has to solve the time-dependent Schrödinger equation

$$i\hbar \frac{\partial}{\partial t} \Psi(\{\mathbf{r}_i\}, \{\mathbf{R}_I\}; t) = H \Psi(\{\mathbf{r}_i\}, \{\mathbf{R}_I\}; t). \tag{2.18}$$

This is virtually impossible without significant approximations. Even approximative methods are computationally expensive and, in many cases, too simplified to give accurate results. This is why most of the molecular dynamics studies up to date have been based on predefined potentials constructed from empirical data or electronic structure calculations for fixed systems. The advantages of these classical molecular dynamics methods are obvious. They are fast compared to the the quantum mechanical methods, and it is possible to adjust them. This gives an experimental aspect through the possibility of playing with the potentials, and makes it easier to understand the behavior of many-particle systems. The predefined potentials suffer, however, from major drawbacks. The parametrization becomes very complicated in systems with many types of atoms, where different kinds of interatomic interactions have to be taken into account. Furthermore, classical methods cannot provide information about the electronic structure, and cannot describe chemically complex systems where the bonding pattern changes during the simulation (bond breaking/formation) [22].

Drawbacks in the classical molecular dynamics methods encouraged the development of the so-called *ab initio* methods which are based on quantum mechanics, and have a truly predictive power as the electronic structure and the forces acting on nuclei are examined in parallel at each time step during the dynamics. Methods directly based on the time-dependent Schrödinger equation (2.18) are demanding in practice, because the time evolution of electrons and nuclei have to be solved simultaneously. The electronic movement is fast compared to that of the nuclei, and numerous time steps are needed in order to see any significant changes in the atomic positions. This is the reason why intermediate methods have been developed. The two methods applied in this thesis are introduced next. First is the Born-Oppenheimer method, which is based on the time-independent Schrödinger equation and classical forces, and the second is the Car-Parrinello molecular dynamics, in which the quantum dynamics of slow nuclei and fast electrons is mapped onto a purely classical problem.

Born-Oppenheimer molecular dynamics is based on the BO approximation introduced in Section (2.2), and does not involve solving the time-dependent Schrödinger equation. The core of the method are the equations [22]:

$$M_I \ddot{\mathbf{R}}_I(t) = -\nabla_I min_{\Psi_0} \{ \langle \Psi_0 | H_e | \Psi_0 \rangle \} \tag{2.19}$$

$$H_e \Psi_0 = E_0 \Psi_0, \tag{2.20}$$

where min_{Ψ_0} means a minimization with respect to the states Ψ_0. Equation (2.19) gives the forces acting on nuclei, which are used to determine the movement of nuclei,

and the ground-state electronic structure has to be calculated after every time step from Eq. (2.20). One should note, that $-\nabla_I\{\langle\Psi_0|H_e|\Psi_0\rangle\}$ is exactly the Hellman-Feynman force (Eq. (2.11)) provided that the wavefunction Ψ_0 is an exact eigenfunction [22].

Born-Oppenheimer molecular dynamics has been applied succesfully, for example, by Robert N. Barnett and Uzi Landman (1993), whose method was originally based on the local-spin-density approximation, non-local, norm-conserving pseudopotentials and a plane-wave basis (see Chapter 3) [23]. Remarkable in this method is that it does not employ periodic boundary conditions (PBCs), which makes it more applicable for charged systems or systems with large multipole moments. For methods using PBCs, the interaction between the periodically repeated replicas can affect results significantly.

Another, not so obvious but much applied method was developed by Roberto Car and Michele Parrinello in 1985 [24]. In the Car-Parrinello (CP) method, the self-consistent electronic optimization is not done after each molecular dynamics step. However, the method makes it possible to use larger time step than in the methods based on the first order time-dependent Schrödinger equation. In classical mechanics, the force on nuclei is obtained from the derivative of a Lagrangian with respect to the nuclear positions. The energy of the electronic subsystem, $\langle\Psi_0|E_e|\Psi_0\rangle$ is a function of both nuclear positions $\{\mathbf{R_I}\}$ and single-particle orbitals $\{\psi_i\}$, and Car and Parrinello suggested that a functional derivative with respect to the orbitals gives the force acting on the orbitals if a suitable Lagrangian is chosen.

Car and Parrinello postulated the Lagrangian of the form

$$L_{CP} = \sum_I \frac{1}{2}M_I\dot{\mathbf{R}}_I^2 + \sum_i \frac{1}{2}\mu_i\langle\dot{\psi}_i|\dot{\psi}_i\rangle - \langle\Psi_0|H_e|\Psi_0\rangle + constraints, \qquad (2.21)$$

where the first two terms are the kinetic energy of nuclei and electrons, third term is the potential energy, and the last assures the orthonormality of orbitals. The inertia parameters μ_i can be described as fictitious masses of the orbitals ψ_i, and constraints are needed because of the orthonormality requirement etc. The associated Euler-Lagrange equations

$$\frac{d}{dt}\frac{\partial L}{\partial\dot{\mathbf{R}}_I} = \frac{\partial L}{\partial\mathbf{R}_I} \qquad (2.22)$$

$$\frac{d}{dt}\frac{\delta L}{\delta \dot{\psi}_i^*} = \frac{\delta L}{\delta \psi_i^*}, \tag{2.23}$$

result in the Newtonian equations of motion, i.e. the Car-Parrinello equations of the form

$$M_I \ddot{\mathbf{R}}_I(t) = -\frac{\partial}{\partial \mathbf{R}_I}\langle \Psi_0|H_e|\Psi_0\rangle + \frac{\partial}{\partial \mathbf{R}_I}\{constraints\} \tag{2.24}$$

$$\mu_I \ddot{\psi}_i(t) = -\frac{\delta}{\delta \psi_i^*}\langle \Psi_0|H_e|\Psi_0\rangle + \frac{\delta}{\delta \psi_i^*}\{constraints\}, \tag{2.25}$$

where the constraints are holonomic [24], and depend on $\{\psi_i\}$ and $\{\mathbf{R}_I\}$. It should be emphasized that the electron dynamics above is fictitious, and it is introduced in order to get realistic nuclear dynamics.

Making a choice between the BO and Car-Parrinello molecular dynamics is not an obvious decision [22]. In the Car-Parrinello molecular dynamics, the electronic degrees of freedom are treated together with nuclear dynamics at each time step, and as the equations of motion for nuclei and electrons are coupled the time step has to be reasonably small. In the BO molecular dynamics, the electron dynamics is absent, which is formally an order of magnitude advantage with respect to the CP molecular dynamics, at least if the nuclear motion is slow. On the other hand, the electronic structure has to be minimized for each nuclear configuration in the BO molecular dynamics. The longer the time step used, the longer the electronic optimization takes as the wavefunction calculated during the previous time step (initial guess for the minimization) is further away from the new one.

In the first article of this thesis [I], we apply the Born-Oppenheimer local-spin-density molecular dynamics (BO-LSD-MD) program developed by Robert N. Barnett and Uzi Landman [23]. In this method, the ions move according to classical mechanics, and the forces are calculated using the generalized gradient-corrected approximation (GGA) for the exchange-correlation energy functional and pseudopotentials that describe the ion cores (see Section 3.5). The electron density as well as the orbitals are expanded using a plane wave basis set (see Section 3.4). The applied BO-LSD-MD method does not use periodic boundary conditions, and it is therefore an appropriate method for isolated clusters with considerable charges or multipole moments.

In the last three articles of this thesis [II]-[IV], we apply the Car-Parrinello molecular dynamics (CPMD) [24] code originally introduced by Roberto Car and Michele Parrinello (see [25] for the latest version of the code) which applies periodic boundary conditions, GGA for the exchange-correlation energy functional, and pseudopotentials. Again, plane waves are used as basis functions for the electron density and orbitals. Due to the fact that CPMD uses PBCs it is a natural choice for periodic structures (in this thesis the semimetallic graphite surface and carbon nanotubes), and its usage is justified for neutral clusters. In fact, the current implementation includes an option where PBCs can be switched off, which enables simulations of finite charged systems as well. On the other hand, the finite system calculations can produce incorrect results for macroscopic objects (surfaces, bulk) which have a band structure.

3 Density Functional Theory: Basics and Implementation

3.1 Hohenberg-Kohn Theorems

The Hamiltonian H_{elec} of an N-electron system can be written in the form

$$H_{elec} = T + U_{ee} + V_{ext}, \tag{3.1}$$

where T is the kinetic energy part of electrons, U_{ee} is the energy related to the electron-electron Coulombic repulsion, and V_{ext} is the energy related to the interaction between electrons and an external potential $v(\mathbf{r})$ which includes the potentials caused by nuclei and external fields. The $T + U_{ee}$ part is universal to all N-electron systems, and the external potential part V_{ext} fixes the Hamiltonian. Thus, N and $v(\mathbf{r})$ determine all the properties of the ground state. If the Hamiltonian H of the electronic system is known, then the ground-state energy and wave function can be, in principle, determined by minimizing the energy functional $E[\Psi]$ with respect to Ψ. It was the idea of Hohenberg and Kohn to replace N and $v(\mathbf{r})$ as basic variables with the electron density $\rho(\mathbf{r})$, which can be written in the form

$$\rho(\mathbf{x}_1) = N \int \int \ldots \int |\Psi(\mathbf{x}_1, \mathbf{x}_2, \ldots, \mathbf{x}_N)|^2 d\mathbf{x}_2 \ldots d\mathbf{x}_N, \tag{3.2}$$

where $d\mathbf{x}_i$ includes differentials with respect to coordinates and spin, and N is the total number of electrons

$$N = \int \rho(\mathbf{r}) d\mathbf{r}, \tag{3.3}$$

when Ψ is normalized. The energy functional is then

$$E[\rho] = \langle \Psi[\rho]|H|\Psi[\rho]\rangle = \langle \Psi[\rho]|T + U_{ee} + V_{ext}|\Psi[\rho]\rangle = F[\rho] + \int \rho(\mathbf{r})v(\mathbf{r})d\mathbf{r}, \tag{3.4}$$

15

where $F[\rho] = \langle \Psi[\rho]|T + U_{ee}|\Psi[\rho]\rangle$ is a universal functional for all N-electron systems. This method where the energy is minimized as a functional of the electron density, is called as the Density Functional Theory (DFT).

The first Hohenberg-Kohn theorem legitimizes the use of ρ instead of N and Ψ [26]; it says that *the external potential $v(\mathbf{r})$ is determined, within a trivial additive constant, by the electron density $\rho(\mathbf{r})$*. As N is determined by integrating ρ over space, it follows that ρ also determines the ground-state wave function Ψ and all the electronic properties of the system. The proof of this theorem is very easy, if we assume that the ground state of an N-electron system is nondegenerate. This assumption is not necessary if the problem is investigated in detail, but by now it alleviates the procedure.

Let us assume that there are two Hamiltonians H and H' with potentials v and v', which differ more than by a constant. Each Hamiltonian gives the same ρ for its ground state although the normalized wave functions Ψ and Ψ' are different. By Eq. (2.13) we then have

$$E_0 < \langle \Psi'|H|\Psi'\rangle = \langle \Psi'|H'|\Psi'\rangle + \langle \Psi'|H - H'|\Psi'\rangle = E_0' + \int \rho(\mathbf{r})[v(\mathbf{r}) - v'(\mathbf{r})]d\mathbf{r}, \quad (3.5)$$

where E_0 and E_0' are the ground-state energies for H and H', respectively. On the other hand

$$E_0' < \langle \Psi|H'|\Psi\rangle = \langle \Psi|H|\Psi\rangle + \langle \Psi|H' - H|\Psi\rangle = E_0 - \int \rho(\mathbf{r})[v(\mathbf{r}) - v'(\mathbf{r})]d\mathbf{r}. \quad (3.6)$$

By adding these two equation together we get $E_0 + E_0' < E_0' + E_0$, which is contradictory, and thus, there cannot be two different v that give the same ρ for their ground states. Consequently, ρ determines N and v unambiguously as well as all the properties of the ground state.

The second Hohenberg-Kohn theorem provides the variational principle by stating that *for a trial density $\tilde{\rho}(\mathbf{r}) \geq 0$,*

$$E_0 \leq E[\tilde{\rho}], \quad\quad\quad\quad\quad\quad (3.7)$$

where $E[\tilde{\rho}]$ is the total energy functional, and $\int \tilde{\rho}(\mathbf{r})d\mathbf{r} = N$.

The so-called v-representable electron density is associated with the antisymmetric ground-state wave function of a Hamiltonian with some external potential $v(\mathbf{r})$. There

are electron densities that are not v-representable, but most studies are restricted to the v-representability where there exists one-to-one mapping between the electron density and external potential. In practice, the requirements are further weakened as one replaces the v-representability by a condition that is called as the N-representability, which means that $\rho(\mathbf{r})$ is obtained from some antisymmetric wave function that fulfills the following requirements:

$$\rho(\mathbf{r}) \geq 0, \int \rho(\mathbf{r})d\mathbf{r} = N, \text{ and } \int |\nabla\rho(\mathbf{r})^{\frac{1}{2}}|^2 d\mathbf{r} < \infty. \tag{3.8}$$

3.2   Kohn-Sham Method

The most practical implementation of DFT was introduced by Kohn and Sham in 1965 [27]. Their idea was to study first noninteracting electrons for which the Hamiltonian is

$$H_s = \sum_{i=1}^{N} h_i = \sum_{i=1}^{N} [-\frac{1}{2}\nabla_i^2 + v_s(\mathbf{r})], \tag{3.9}$$

where the external potential v_s for a single particle is in this context the Coulomb potential of ion cores.

The wave-function solved from the Schrödinger equation is then of the form of Eq. (2.15), and it is constructed from the N lowest one-electron states ψ_i that satisfy the equations

$$h_i\psi_i = [-\frac{1}{2}\nabla_i^2 + v_s(\mathbf{r})]\psi_i(\mathbf{r}) = \varepsilon_i\psi_i(\mathbf{r}). \tag{3.10}$$

From these single-particle equations, the electron density

$$\rho(\mathbf{r}) = \sum_{i=1}^{N} |\psi_i(\mathbf{r})|^2, \tag{3.11}$$

can be achieved. The idea of the Kohn-Sham (KS) method is to apply the exact kinetic energy functional of the noninteracting system,

$$T_s[\rho] = \sum_{i=1}^{N} \langle \psi_i | -\frac{1}{2}\nabla^2 | \psi_i \rangle, \tag{3.12}$$

in the case of interacting electrons. The corresponding energy functional is then

$$E[\rho] = T_s[\rho] + V_{ne}[\rho] + J[\rho] + E_{xc}[\rho], \tag{3.13}$$

where

$$V_{ne}[\rho] = \int v(\mathbf{r})\rho(\mathbf{r})d\mathbf{r} \tag{3.14}$$

$$J[\rho] = \frac{1}{2}\int\int \frac{\rho(\mathbf{r_1})\rho(\mathbf{r_2})}{r_{12}}d\mathbf{r_1r_2} \tag{3.15}$$

$$E_{xc}[\rho] = \langle \Psi | T + U_{ee} | \Psi \rangle - T_s[\rho] - J[\rho] \tag{3.16}$$

are the the energy related to the interaction between electrons and an external potential ($V_{ne}[\rho]$), the classical electron-electron repulsion ($J[\rho]$), and the exchange and correlation ($E_{xc}[\rho]$). The Euler-Lagrange equation can be written in the form

$$\mu = \frac{\delta E[\rho]}{\delta \rho(\mathbf{r})} = v_{eff}(\mathbf{r}) + \frac{\delta T_s[\rho]}{\delta \rho(\mathbf{r})}, \tag{3.17}$$

if we identify

$$v_{eff}(\mathbf{r}) =: \frac{\delta V_{eff}[\rho]}{\delta \rho(\mathbf{r})} = v(\mathbf{r}) + \frac{\delta J[\rho]}{\delta \rho(\mathbf{r})} + \frac{\delta E_{xc}}{\delta \rho(\mathbf{r})} = v(\mathbf{r}) + \int \frac{\rho(\mathbf{r}')}{|\mathbf{r}-\mathbf{r}'|}d\mathbf{r}' + v_{xc}(\mathbf{r}), \quad (3.18)$$

where

$$V_{eff}[\rho] = V_{ne}[\rho] + J[\rho] + E_{xc}[\rho]. \tag{3.19}$$

Now, v_{eff} has a similar role as v_s in the case of noninteracting electrons, and we obtain $\rho(\mathbf{r})$ that satisfies Eq. (3.17) by solving the N single-particle equations

$$\{-\frac{1}{2}\nabla_i^2 + v_{eff}(\mathbf{r})\}\psi_i(\mathbf{r}) = \varepsilon_i\psi_i(\mathbf{r}), \tag{3.20}$$

and setting

$$\rho(\mathbf{r}) = \sum_{i=1}^{N} |\psi_i|^2. \tag{3.21}$$

As v_{eff} depends on ρ, Eqs. (3.18)-(3.21) have to be solved self-consistently. In practice, this means that a constructed trial density is used to determine v_{eff} in Eq. (3.18), which is then used to obtain $\rho(\mathbf{r})$ from Eqs. (3.20) and (3.21), the obtained $\rho(\mathbf{r})$ is used as a new trial density, and the whole procedure is repeated. This is done until the results converge (self-consistency) after which the total energy can be calculated from Eq. (3.13).

The electron spin can be taken into consideration in the KS method by defining that the electron density is $\rho(\mathbf{r}) = \rho_\downarrow(\mathbf{r}) + \rho_\uparrow(\mathbf{r})$, where $\rho_\downarrow(\mathbf{r})$ and $\rho_\uparrow(\mathbf{r})$ are the densities of spin down and spin up electrons, respectively, and

$$\rho_\sigma(\mathbf{r}) = \sum_{i=1}^{N_\sigma} |\psi_{i\sigma}|^2, \tag{3.22}$$

where N_σ is the number of electrons with spin $\sigma = (\uparrow, \downarrow)$. In this case, we have the KS equations with orbitals $\psi_{i\sigma}$, and energies $\varepsilon_{i\sigma}$ for both spins, and v_{eff} in Eq. (3.18) depends on the spin as $v_{xc}^\sigma = \delta E_{xc}/\delta\rho_\sigma(\mathbf{r})$.

3.3 Local Density and Gradient Corrected Approximations

The Kohn-Sham equations (3.18)-(3.21) are formally exact. The problem is, however, that the explicit form of the exchange-correlation energy $E_{xc}[\rho]$ is unknown. It has become evident that the search of an accurate $E_{xc}[\rho]$ is the greatest challenge in DFT [21] although several succesful approximations have been developed. Qualitatively succesful yet simple approximation for $E_{xc}[\rho]$ is the local-density approximation (LDA)

$$E_{xc}^{LDA}[\rho] = \int \rho(\mathbf{r})\varepsilon_{xc}(\rho)d\mathbf{r}, \tag{3.23}$$

where $\varepsilon_{xc}(\rho)$ is the exchange-correlation energy per particle of the uniform electron gas with density ρ. This energy can be divided into separate exchange and correlation

parts,

$$\varepsilon_{xc}(\rho) = \varepsilon_x(\rho) + \varepsilon_c(\rho). \tag{3.24}$$

The exchange part of the uniform electron gas can be calculated using the Hartree-Fock theory [28], and the correlation function can be interpolated based on the accurate values received from the quantum Monte Carlo calculations [21]. In the spin-dependent case the exchange-correlation energy $\varepsilon_{xc}(\rho, \xi)$ depends on the polarization $\xi = (\rho_\uparrow - \rho_\downarrow)/\rho$, and can be written in the form

$$\varepsilon_{xc}(\rho, \xi) = \varepsilon_{xc}(\rho, 0) + f(\xi)[\varepsilon_{xc}(\rho, 1) - \varepsilon_{xc}(\rho, 0)], \tag{3.25}$$

where $f(\xi)$ gives the polarization dependence between the fully polarized ($\xi = 1$) and unpolarized ($\xi = 0$) limits. The method where the spin is taken account is called as the local spin-density approximation (LSD). Because of the nature of the LDA (or LSD) method, one would expect that it gives good results only for systems where the electron density is nearly uniform. However, calculations have proved that LDA gives surprisingly realistic results also for systems with a considerable variation in the electron density.

The generalized gradient-corrected approximation (GGA) was developed in order to improve the LSD method. The density inhomogeneties in E_{xc} are taken into account by including the gradients of the spin-densities. In practice, only a few terms are included in the gradient expansion, and slowly varying or small density variations are described less satisfactorily [29]. This is problematic, for example, with the pseudopotential theory of simple metals where the linear-response limit is physically important.

A parametrized analytic form of ε_{xc} is well established in the LSD method, but the best description of the gradient correction is still under debate. A functional that was designed to catch the energetically significant features was introduced by Perdew *et al.* in 1996 [29], and it is referred to as the PBE functional. It describes the uniform electron gas better than the earlier GGA methods, it is constructed so that it gives physical results in the limits, and it has an analytical form which has improved the numerical efficiency compared to the earlier forms, such as the one made by Perdew and Wang in 1991 [30]. In the PBE scheme the correlation energy is of the form

$$E_c^{GGA}[\rho_\uparrow, \rho_\downarrow] = \int d^3r \rho[\varepsilon_c(r_s, \xi) + H(r_s, \xi, t)], \tag{3.26}$$

where r_s is the local Seitz radius ($\rho = 3/4\pi r_s^3 = k_F^3/3\pi^2$), $\xi = (\rho_\uparrow - \rho_\downarrow)/\rho$ is the

relative spin polarization, and $t = |\nabla\rho|/2\phi k_s \rho$ is a dimensionless density gradient, where $\phi(\xi) = [(1+\xi)^{2/3} + (1-\xi)^{2/3}]/2$ is a spin-scaling factor, and $k_s = \sqrt{4k_F/\pi a_0}$ is the Thomas-Fermi Screening wave number ($a_0 = \hbar^2/me^2$). The gradient contribution

$$H = (e^2/a_0)\gamma\phi^3 \times \ln\{1 + \frac{\beta}{\gamma}t^2[\frac{1 + At^2}{1 + At^2 + A^2t^4}]\}, \tag{3.27}$$

where

$$A = \frac{\beta}{\gamma}[\exp\{-\varepsilon_c/(\gamma\phi^3 e^2/a_0)\} - 1]^{-1}, \tag{3.28}$$

and β and γ are adjustable parameters, gives realistic results in the slowly varying, in the rapidly varying and in the high-density limits. The corresponding exchange energy is written as

$$E_X^{GGA} = \int d^3 r \rho \varepsilon_x(\rho) F_X(s), \tag{3.29}$$

where $\varepsilon_x = -3e^2 k_F/4\pi$ and the so-called spin-polarized enhancement factor F_X is

$$F_X(s) = 1 + \kappa - \kappa/(1 + \mu s^2 \kappa), \tag{3.30}$$

where κ and μ are parameters. The PBE gradient corrected method described above should produce the most important features of the real exchange-correlation energy. It takes into account the rapid density variations as a GGA method should, and in the limit of uniform electron gas it behaves as the LSD method which is formally correct.

3.4   Plane Wave Basis

The application of the KS method requires fi auxiliary single-particle wave functions. The explicit form of the KS wave functions is, however, yet to be defined. They can be represented by a basis set which consists of simple analytic functions f_ν with well-known properties. In general, the expansion form of a periodic function ψ_i with respect to certain basis functions can be written as a linear combination

$$\psi_i(\mathbf{r}) = \sum_\nu c_{i\nu} f_\nu(\mathbf{r}; \{\mathbf{R}_I\}), \tag{3.31}$$

where $c_{i\nu}$ are the orbital expansion coefficients. In quantum chemistry, the atom centered Slater- or Gaussian-type basis functions have been typically used [22]. However, a completely different approach which is suggested by the solid state theory of periodic lattices is adopted here. Periodic boundary conditions impose periodicity on the electron density. This implies that a plane wave basis might be a convenient choice as the generic basis set for expanding the periodic part of the orbitals as in the Bloch's Theorem. Plane waves are an appropriate choice as they form a complete and orthonormal set of functions. The plane wave basis functions can be written as

$$f_\mathbf{G}^{PW}(\mathbf{r}) = \frac{1}{\sqrt{V}} \exp[i\mathbf{G} \cdot \mathbf{r}], \tag{3.32}$$

where $\mathbf{G}$ is a reciprocal vector, $\mathbf{r}$ is a real space vector, and V is the volume of the periodic super-cell. By using plane waves with periodic boundary conditions, a periodic wave function can be expanded into the form

$$\psi(\mathbf{r}) = \psi(\mathbf{r} + \mathbf{L}) = \frac{1}{\sqrt{V}} \sum_\mathbf{G} \psi(\mathbf{G}) \exp[i\mathbf{G} \cdot \mathbf{r}], \tag{3.33}$$

where $\psi(\mathbf{r})$ and $\psi(\mathbf{G})$ are related by a three-dimensional Fourier transform, and $\mathbf{L}$ is a direct lattice vector connecting the equivalent points in different cells [22]. Furthermore, the KS orbitals can be written as

$$\phi_i(\mathbf{r}, \mathbf{k}) = \frac{1}{\sqrt{V}} \sum_\mathbf{G} c_i(\mathbf{G}, \mathbf{k}) \exp[i(\mathbf{G} + \mathbf{k}) \cdot \mathbf{r}], \tag{3.34}$$

where $\mathbf{k}$ is a vector in the first Brillouin zone, and $c_i(\mathbf{G}, \mathbf{k})$ are complex numbers. Now, the expanded form of the density is

$$\begin{aligned}
n(\mathbf{r}) &= \frac{1}{\sqrt{V}} \sum_i \int d\mathbf{k} f_i(\mathbf{k}) \sum_{\mathbf{G}, \mathbf{G}'} c_i^*(\mathbf{G}', \mathbf{k}) c_i(\mathbf{G}, \mathbf{k}) \exp[i(\mathbf{G} + \mathbf{k}) \cdot \mathbf{r}] \\
&= \sum_\mathbf{G} n(\mathbf{G}) \exp[i\mathbf{G} \cdot \mathbf{r}], \tag{3.35}
\end{aligned}$$

where the sum over i runs over all the states, and the last sum over $\mathbf{G}$ vectors expands over douple the range given by the wavefunction expansion. In reality, the infinite sums over $\mathbf{G}$ and different cells have to be truncated, and the integral over the Brillouin zone has to be approximated by a finite sum over special $\mathbf{k}$-points

$$\int d\mathbf{k} \rightarrow \sum_{\mathbf{k}} w_k, \tag{3.36}$$

where w_k are the weights of the integration points. The validity of the truncation is based on the fact that the KS potential $v_{eff}(\mathbf{G})$ converges rapidly with increasing the modulus of $\mathbf{G}$. This is why only the vectors $\mathbf{G}$ fulfilling the kinetic energy cutoff condition

$$\frac{1}{2}|\mathbf{k} + \mathbf{G}|^2 \leq E_{cut} \tag{3.37}$$

are included at each $\mathbf{k}$ point.

Plane waves are originless functions, which means that there is no dependence on the position of the nuclei $\{\mathbf{R}_I\}$. Thus, as long as the electronic system has converged to the ground state plane waves do not cause an error called the Pulay force, that is caused by the incomplete basis set in the case of nuclear position dependend functions such as the atom centered functions mentioned previously [35]. The fact, that plane waves are delocalized in space means also that they do not favor certain regions over others, and they form a balanced and reliable basis. Another good feature is that differential operators in the real-space are simply multiplications in the reciprocal space, and both spaces can be efficiently connected via the Fast Fourier Transforms (FFTs). On the other hand, the only way to improve the quality of the basis set is to add more basis functions, as the basis functions can not be shuffled into regions where they are needed the most. This is a problem with structures with strong inhomogeneities, such as complex supermolecules with large empty caps between the branches of the molecule.

3.5   Pseudopotentials

Electronic orbitals feature strong and rapid oscillations close to the nuclei due to the Pauli exclusion principle, which enforces a nodal structure onto the wave function

through orthogonality of the orbitals. Representing these rapid oscillations in the plane wave basis is problematic, which has motivated the development of the so-called pseudopotential approximation [31].

The physical properties of atoms, especially their chemical reactivity, are governed by the valence electrons. This together with the fact that numerically the most consuming problem of the many-body calculations is to calculate the coulombic interaction between electrons has encouraged to develop the pseudopotential approximation, in which the ionic core of an atom (core electrons and nucleus) is described by an effective potential. In other words, the description of the complicated nodal structure in the region of atom cores is avoided by replacing the actual potential of the nucleus and core electrons by an effective potential that produces the same usually smoothly varying plane wave-like wavefunctions outside the core region [32].

Pseudopotentials can be constructed empirically by fitting theoretical results to experiments, or by the more advanced *ab initio* methods, where the pseudopotentials are constructed from the quantum mechanical principles. One of the most simple pseudopotentials is given by the so-called Empty Core Model (ECM), where the unscreened pseudopotential is taken to be zero inside a radius R_e:

$$U(r) = \begin{cases} 0 & , \ for \ \ r < R_e \ \ ; \\ -e^2/r & , \ for \ \ r > R_e \ \ . \end{cases} \tag{3.38}$$

Modern *ab initio* pseudopotentials are constructed by using a spherical screening approximation, and solving self-consistently the radial Kohn-Sham equations [33]

$$[-\frac{1}{2}\frac{d^2}{dr^2} + \frac{l(l+1)}{2r^2} + V[\rho;r]]rR_{nl}(r) = \varepsilon_{nl}rR_{nl}(r), \tag{3.39}$$

where

$$V[\rho;r] = -\frac{Z}{r} + V_H[\rho;r] + V_{xc}(\rho(r)) \tag{3.40}$$

is the self-consistent one-electron potential. The exchange-correlation potential $V_{xc}(\rho(r))$ is usually taken from LDA (GGA in this thesis), ρ is the sum of the electron densities of the occupied wave functions $R_{nl}(r)$, and V_H is the Hartree potential. There are usually four criteria for the pseudopotentials constructed this way [33]. The first one is that

the valence pseudo-wave-functions generated from the pseudopotentials should not contain nodes, i.e. the pseudopotentials should be smooth. Secondly, the normalized atomic radial pseudo-wave-function has to be equal to the corresponding all-electron wave function beyond a chosen cutoff radius r_{cl}, or it should converge rapidly towards that value. Thirdly, the charge enclosed within r_{cl} for the two wave functions should be equal. Finally, the valence all-electron and pseudopotential eigenvalues must be equal. Pseudopotentials fulfilling these requirements are called the "norm-conserving pseudopotentials".

The ultrasoft pseudopotentials have been developed to improve the transferability (i.e. the applicability in various physical and chemical environments) of pseudopotentials [34]. For the ultrasoft pseudopotentials the norm-conserving constraint does not apply, which makes it possible to make nodal structure of the potential even smoother and use less plane-waves with an increased r_{cl}.

4 Results

4.1 Small Magnesium Clusters

Certain properties of small clusters (e.g. structure) are challenging to study experimentally in a systematic manner. This is why theoretical calculations are needed. Theory can help the experiments in focusing on interesting effects, predict achievable structures, and provide interpretation for the measured data. In small particles, however, quantum mechanical effects play an important – if not governing – role, which requires that computationally demanding *ab initio* methods have to be used. This calls for approximative methods as it is a well-known fact that solving the exact many-body Schrödinger equation is practically impossible for more than a few atoms.

The first problem is to find the right cluster geometry. The more atoms there are in the cluster the more possible geometries it can adopt. These configurations which represent local minima of the potential energy surface are separated from each other by energy barriers, and the system can get easily trapped into one of these valleys. Finding the ground-state geometry that corresponds to the global minimum of the potential energy surface is thus increasingly difficult.

For small magnesium clusters the pursuit of finding the global minimum can be handled with the so-called simulated annealing strategy, where molecular dynamics is performed at high temperature so that the atoms are extremely mobile. Time-to-time the cluster is cooled down to a local minimum, and the geometries that are energetically favorable can then be selected as starting geometries for more thorough DFT simulations. Geometries obtained from other sources (intuition, genetic algorithm) should be tried as well, because the simulated annealing procedure does not necessarily give all the low-energy geometries. However, this way there is a better chance to find the global minimum amongst the ever increasing group of different geometries.

In this section, the results for the neutral and cationic magnesium clusters in the size range Mg_2-Mg_{13}, as well as the anionic clusters of the size range Mg_8-Mg_{13}, are discussed. The electronic structure calculations were made with the BO-LSD-MD method described previously in Section 2.4. With small anions this method results in positive highest occupied molecular orbital (HOMO) eigenenergies, which is the reason why only Mg_8 and the larger clusters are considered. The main theme of this work (article [I]) was to investigate the metallic evolution in small magnesium clusters.
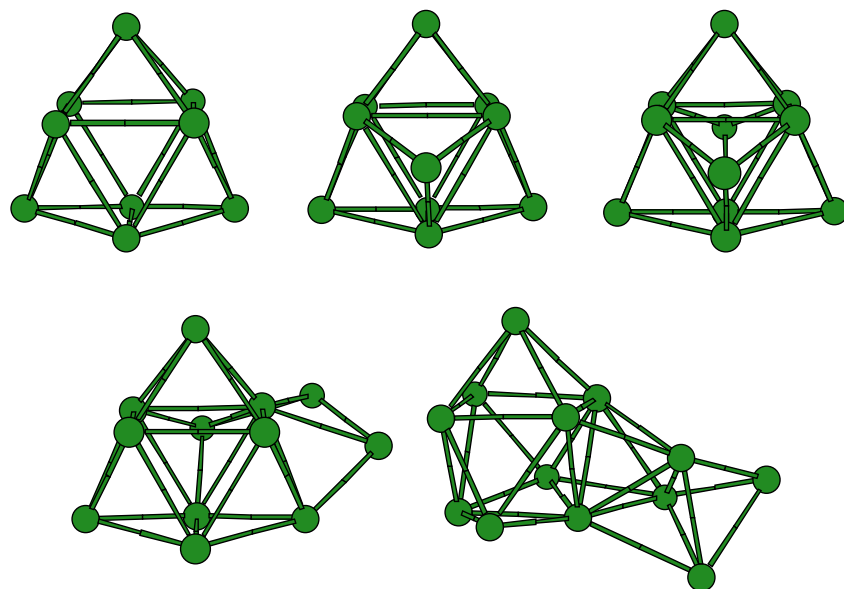
Figure 4.1: The lowest energy structures of Mg$_9$-Mg$_{13}$ clusters. Note the presence of the trigonal prism unit in all the clusters.

It was discovered that the insulator-to-metal transition is not a monotonic function of the cluster size, it is not completed within the size-range studied, and that it is difficult to find a reliable indicator for metallization. However, the evolution of various features in combination can be used as an indicator, especially because our results follow the same trends that were found in the experimental [36] and theoretical [37, 38] studies published soon afterwards.

The ground state structures of neutral magnesium clusters in the size range Mg$_4$-Mg$_8$ are found to be based on a tetrahedron or fused tetrahedrons. Furthermore, Mg$_7$ and Mg$_8$ can be described as a decahedron (bicapped pentagon) and capped decahedron, respectively. In the size range Mg$_9$-Mg$_{13}$, the structures are based on a trigonal prism (see Fig. 4.1). These geometries agree well with the earlier studies [39, 40, 41], although for Mg$_{12}$ and Mg$_{13}$ slightly different isomers were found to be energetically favorable. Later studies confirmed our results [37, 38]. Structures of the cationic clusters are mainly based on the geometries of the neutral clusters but there are also some differences. The small cations appear linear until Mg$_4^+$, and both Mg$_9^+$ and Mg$_{10}^+$ are based on the tetrahedron (or decahedron), whereas the neutral clusters are based on the trigonal prism, and even the energetically most favorable structures of Mg$_{11}^+$ and Mg$_{12}^+$ are slightly different from the corresponding neutral geometries.

In many cases, the energy variation between different isomers is so small that the differences could be within the calculational error. The anionic clusters studied (Mg_8^--Mg_{13}^-) adopted neutral cluster ground state structures with the exception of Mg_{11}^- for which the most stable isomer differs slightly from that of the neutral cluster.

The evolution of the Mg cluster properties is shown in Fig. 4.2. The figure shows the trends in binding energy (E_b), HOMO-LUMO gap (E_g), vertical ionization potential (vIP) and average nearest neighbour distance ($\langle d \rangle$) as a function of the cluster size. The second derivative of the total energy of a cluster with N atoms

$$-\Delta^2 E = (E_{N+1} - E_N) + (E_{N-1} - E_N) = E_{N+1} + E_{N-1} - 2E_N, \qquad (4.1)$$

is shown as an inset. It is a measure of the relative stability of a cluster with respect to the neighboring cluster sizes.

The trends in Fig. 4.2 show that the metallic evolution of Mg clusters is not monotonous. In general, E_b increases, but E_g, vIP and $\langle d \rangle$ decrease as a function of cluster size. The large binding energies (E_b), high relative stability ($-\Delta^2 E$), and compact geometries (small $\langle d \rangle$) of Mg_4 and Mg_{10} fit to the simple jellium picture, according to which they should be "magic" because of their electron numbers 8 and 20 (closed electron shell). The strong binding in Mg_4 and Mg_{10} is also in correlation with the compact geometries of these two. The vertical ionization potentials are of the same magnitude as reported by Jellinek and Acioli [37], but the relative values differ. For example, our trend predicts a dip in vIP for Mg_4, which is in contradiction with the intuition. This suggest that the electron delocalization is different in Mg_4 than in the neighboring cluster sizes. It is also evident that the metallization is still incomplete for the largest cluster size studied (Mg_{13}). Jellinek and Acioli suggested that the p-character of the valence electron density may not be an adequate criterion for the size-induced metallic transition alone, as the degree of p-character is about 50% in bulk magnesium, and it is observed to increase slowly and nonmonotonically when going from a single atom towards the bulk magnesium [37]. Our results for the s- and p-components at the Fermi energy are in agreement with this.
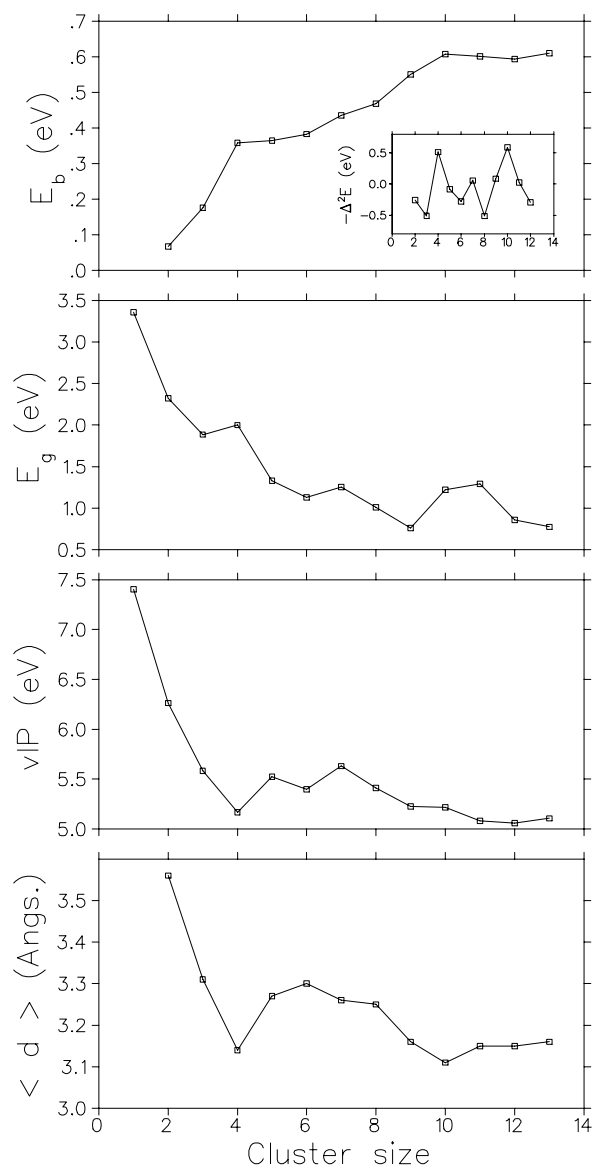
Figure 4.2: Properties of small Mg clusters. From top to bottom: Binding energies (E_b), second derivatives of total energies ($-\Delta^2 E$, inset), HOMO-LUMO gaps (E_g), vertical ionization potentials (vIP) and average nearest neighbour distances ($< d >$).
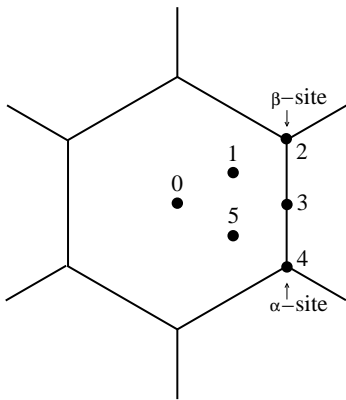
4.2   Alkali Metals on Graphite

Our work on alkali metals on HOPG consists of two articles: The first one concentrates on sodium atoms and clusters [II], while in the second a systematic study of alkali metal atoms, dimers, and monolayers (Li, Na, K, Rb, Cs) is conducted [IV]. In these studies, we used the Car-Parrinello method (see Section 2.4), which employs periodic boundary conditions and is suitable for modelling an infinite graphite surface.

For the sodium calculations [II], we tested various graphite model substrates and calculational methods. First, we studied a finite slab consisting of two to four free graphene "flakes" where the dangling bonds of the peripheral carbons were terminated with hydrogen. The problem with this setup was that the graphene flakes were interlocked (stacking $ABAB...$), and consequently, the system is not symmetric. This irregularity in geometry forced the layers to lean towards each other on the one side and away on the opposite side. Another possible cause of problems could have been that graphite is actually a semimetal with a complicated electronic band structure, and a more proper way to simulate the substrate is an infinite periodic surface.

Next, we applied periodic boundary conditions in an ortorhombic simulation box so that the graphite surface is continuous (infinite) and the adsorbate is replicated periodically on it. The system size and the simulation box had to be large enough so that the interaction between the replicated adsorbates and the replicated graphite slabs in the direction orthogonal to the surface were negligible. Each graphene layer comprised 32 (or 60 in some calculations) carbon atoms in such a manner, that the periodicity formed a continuous surface. The maximum distances between the adsorbate replicas were 9.84 Å and 8.53 Å in the lateral directions, and the perpendicular dimension of the simulation box was chosen so that there was 10-12 Å empty space between the graphite slab replicas. In the charge transfer analysis, it became evident that in order to get rid off the dipole-dipole interaction we had to increase the distance between the slabs up to 20 Å.

Again, two to four graphene layers were tested, and it was found that three layers are needed, as the binding of the Na atom turned out to be sensitive to the number of graphene layers. For two graphene layers, the surface separation is 0.16 Å (6.6%) larger than for three and four layers. In order to incorporate the graphite band structure, different numbers of **k**-points were tried. As a manifestation of the band structure, a twisting of the graphite hexagonal geometry was found upon geometry optimization with only one **k**-point (Γ-point). It was noticed that in order to get the interatomic forces right a 2×2 **k**-point mesh had to be adopted in the lateral dimension, and for the energies a 5×5 **k**-point mesh was needed. In the latter work [IV], we adopted a hexagonal symmetry for the simulation box, after which a 2×2 **k**-point mesh turned out appropriate for calculating the total energies also, and the shortest

Figure 4.3: Numbered locations of alkali metal adatoms on top of a graphite hexagon.

distance between two replicated adatoms became 9.84 Å in both lateral directions. The positions of the carbon atoms were fixed in most simulations in order to reduce the computational cost. Test calculations for Li atoms on graphite, where either four or six nearest carbon atoms were set free, showed that this caused negligible changes in the geometries as well as in the energies.

Among alkali metals, sodium is found to have an anomalous behavior as it interacts relatively weakly with the graphite surface. This is especially evident for Na_2, which has a closed electron shell (two valence electrons), and it resides 3.05-3.95 Å apart from the surface depending on the alignment. The energetics of Na favors clustering processes on HOPG, and the stability of clusters with an open valence electron shell is increased due to the spin-degeneracy of the highest molecular orbital (odd-even staggering). For example, the formation energy of Na_5 is 0.99 eV larger than that of five separate adatoms ($\Delta E = 2.55$ eV), and 0.52 eV larger than the formation energy of separated Na_3 and Na_2. The formation energy is defined as a sum of the adsorption energy per atom ($\Delta E_\perp$) of a cluster/monolayer and the binding energy (E_b) of an atom in a free cluster/monolayer.

The increased stability of the odd cluster sizes and the inertness of Na_2 (closed shell) can be seen from the fact that the most stable configuration of four Na atoms on graphite is the pair Na_3 and Na with a formation energy $\Delta E = 2.56$ eV which is 0.52 eV higher than for four separate adatoms. The lowest formation energy is observed for two separated Na_2 clusters with $\Delta E = 1.92$ eV. The geometries of Na_4 and Na_5 deviated from planarity, but it is not clear whether this is related to the experimentally observed buckling of Na overlayers [42, 43].

All the alkali metal adatoms are found to prefer the hollow site of the hexagonal graphite sublattice (location 0 in Fig. 4.3). Calculations on a few selected locations (all locations in Fig. 4.3 for Na, locations 0, 1, 2, and 4 for the other alkali metal

adatoms) show, that the alkali metal adatoms can diffuse almost freely on the graphite surface, as only lithium has a considerable diffusion barrier ($E_{diff} = 0.21$ eV). This is probably due to the small atomic radius of Li, while for the other alkali metal adatoms the diffusion barrier is almost negligible (E_{diff} 0.02-0.06 eV). Experiments have shown, that Li forms intercalated structures readily, as it penetrates between two graphene sheets and localizes at the hollow site [6].

The trends in the formation/adsorption energy and surface separation of the alkali metal adatoms and (2×2) MLs are shown in Fig. 4.4. A comparison of the formation energies reveals that in most cases the dispersed phase is energetically more stable than (2×2) ML. This is in agreement with the experiments as there is no island formation in the low coverage regime. This is evident as for all the other alkali metals but Na, the formation energy per atom is larger for separate adatoms than for the (2×2) structure. However, when the coverage is increased so that the adatoms become closer to each other the (2×2) construction is preferred for K, and it represents a stable phase for Rb and Cs under certain circumstances [6].

Among the separated adatoms, lithium was found to have the largest adsorption energy $\Delta E_\perp = 1.21$ eV, and sodium the smallest with $\Delta E_\perp = 0.55$ eV. For K, Rb and Cs the adsorption energy grows slowly as the atomic radius increases, $\Delta E_\perp$ being 0.99 eV, 1.02 eV and 1.04 eV, respectively. The distances from the surface grow steadily as the atomic radius increases: Li is closest to the surface with $d_\perp = 1.84$ Å and Cs farthest with $d_\perp = 3.75$ Å. Experimental value $d_\perp = 2.79 \pm 0.03$ Å for a K (2×2) layer [44] is closer to the value $d_\perp = 2.72$ Å that we obtain for a separated K atom than the value $d_\perp = 3.17$ Å of for K (2×2) ML. This difference could be caused by the GGA functional used for the exchange-correlation energy or it could be related to the indirect evaluation method of the experimental layer spacing.

The adsorption energies and the surface separation show that the metal layer undergoes a decoupling from the surface as the coverage is increased. This effect is clearly seen as a drop in the adsorption energies and an increase in the surface separation when comparing separated adatoms with (2×2) MLs. A single potassium atom, for example, has an adsorption energy $\Delta E_\perp = 0.99$ eV, whereas the same for K (2×2) ML is only 0.25 eV per atom. For two monolayers, the adsorption energy is only 0.13 eV per atom, which is one half of the adsorption energy of one layer. This means that the total adsorption energy in the simulation box is the same for one and two layers, and the second overlayer does not interact with the surface. However, the formation energy is almost exactly the same as for 1ML suggesting a stronger interaction between the K atoms as the coverage is increased. The weak interaction between the substrate and metal film is further supported by the fact that the separation of the lower K overlayer ($d_\perp = 3.11$ Å) is almost the same as in the case of one monolayer ($d_\perp = 3.17$ Å).
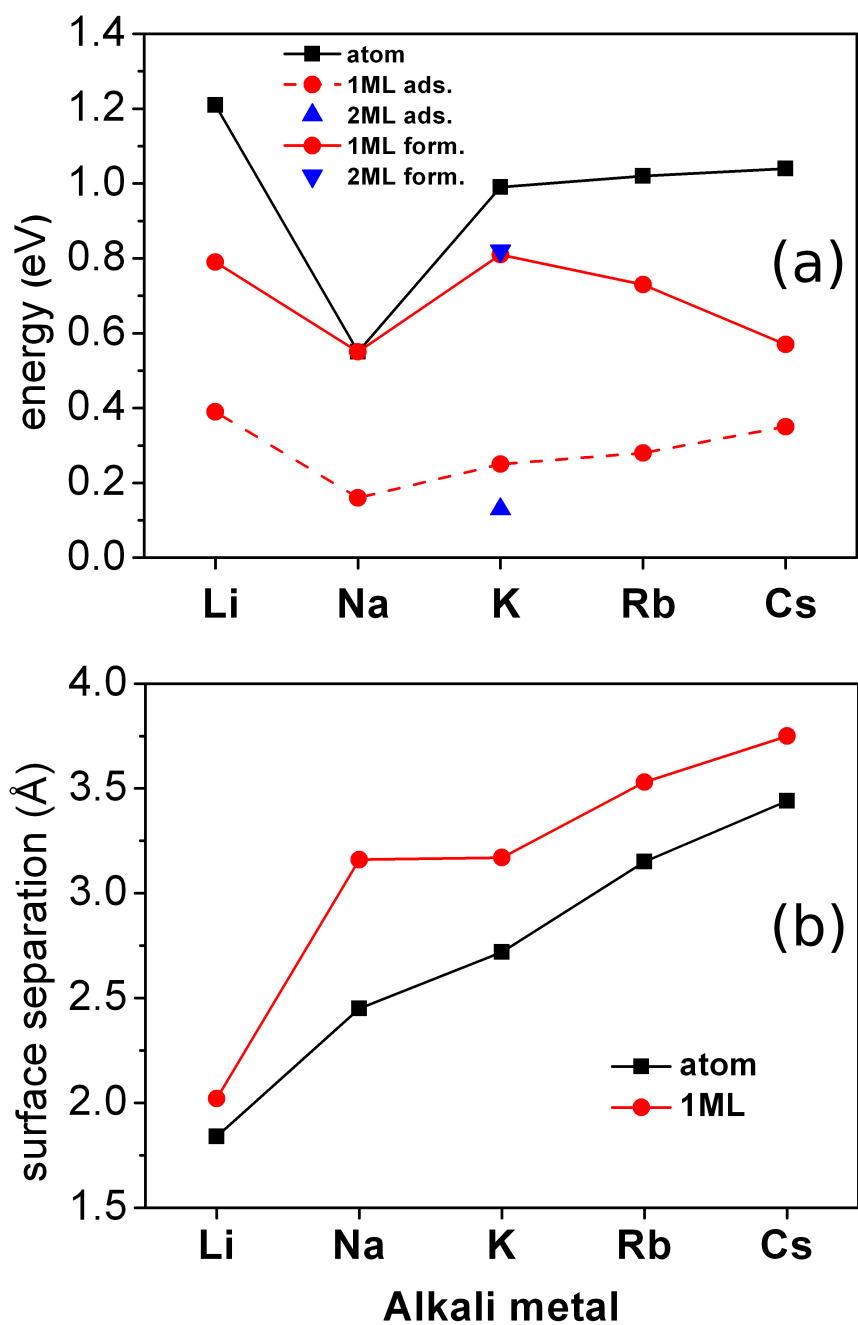
Figure 4.4: Adsorption of alkali metal atoms and (2×2) monolayers on graphite: (a) the formation and adsorption energies per atom (ΔE and $\Delta E_\perp$) and (b) the vertical separation from the substrate ($\Delta E_\perp$).

Table 4.1: Comparison between different DFT methods.

Adsorbate	Functional	ΔE (eV)	$d_\perp$ (Å)	Reference
Li Atom	PBE	1.21	1.84	This work
	PBE (LDA)	1.10 (1.68)	1.71 (1.63)	Ref. [45], slab model
	B3LYP	1.36	1.71	Ref. [46], cluster model
	LDA	1.60	1.64	Ref. [47], slab model
(2×2)	PBE	0.79	2.02	This work
	LDA	0.93	1.64	Ref. [47], slab model
Na Atom	PBE	0.55	2.45	This work
	PBE	0.50 (0.69)	2.34 (2.42)	Ref. [45], slab model
	B3LYP	0.72	2.10	Ref. [46], cluster model
	PW91		2.32	Ref. [48], slab model
K Atom	PBE	0.99	2.72	This work
	PBE (LDA)	0.88 (1.12)	2.65 (2.70)	Ref. [45], slab model
	BP86 (LDA)	1.49 (1.67)	2.81 (2.73)	Ref. [49], cluster model
	B3LYP	1.06	2.51	Ref. [46], cluster model
	LDA	0.51	2.79	Ref. [50], slab model
	LDA	0.78	2.77	Ref. [51], slab model (1 layer)
(2×2)	PBE	0.81	3.17	This work
	LDA	0.98	2.82	Ref. [50], slab model
	LDA	0.48	2.82	Ref. [51], slab model (1 layer)

We have evaluated the amount of charge transfer (Δq) by using the laterally averaged charge density difference ($\Delta\rho_\perp$), where one integrates over the charge depletion area around (below) the alkali metal adatoms (layer). All the alkali metal adatoms donate 0.4-0.5 e to the substrate. For (2×2) MLs, the electron density redistribution upon adsorption is different, and the amount of donated charge is approximately 0.1 e per adatom. Here, it should be noticed that as in the experiments there are several ways to evaluate the charge transfer theoretically, and they can give varying results.

The results for the formation energy and surface separation in comparison with other DFT studies are presented in Tab. 4.1. One can see that our results are mostly in agreement with the other studies, and especially with the slab model calculations where the PBE functional is used [45]. The largest differences are observed with the LDA studies: The LDA formation energy tends to be systematically higher and the distance from the surface lower which is expected as LDA has an over-binding character. Exceptions to this pattern are presented by the LDA slab model calculations of Lamoen and Persson [50] and Ancilotto *et al.* (one graphene layer only) [51], and for example, the value $\Delta E = 0.51$ eV from Ref. [50] is barely one half of the $\Delta E= 0.99$ eV

in our study. The attraction between graphene layers is mainly of the van der Waals character, and it is not reproduced by standard DFT. The over-binding character of LDA gives by chance a more realistic interlayer distance than GGA, and it is often suggested in the literature that LDA should give better results for the adatom binding energies and distances. The difference can also be seen in the $d_\perp$ values when comparing our results to the LDA studies for Li [47] and K [50, 51]. In general, our PBE results are in reasonable agreement with the other studies, and we believe that our results are reliable due to the extensive testing.

Fig. 4.5 shows the laterally averaged charge density difference ($\Delta\rho_\perp$) of a K adatom, (2×2) ML, and two (2×2) overlayers on graphite. It can be seen, that even though the amount of charge transferred to graphite is almost the same, there are significant differences between the three curves. In the case of a separate K atom, charge depletes through the whole atomic volume of K and accumulates mostly over the topmost graphene layer. For a (2×2) monolayer, the charge is depleted below the monolayer which already implies a decoupling tendency. The curves of 1ML and 2ML are practically identical below the lower metal layer. Decoupling is further supported by the charge redistribution of 2ML (accumulation between the K layers), and the corresponding electronic density of valence states (DOS) is essentially a sum over the DOS of the separated metal layer and graphite substrate.

More detailed cutplane visualizations of the charge redistribution are given for lithium in Fig. 4.6, and for two K monolayers in Fig. 4.7. From the upper part of Fig. 4.6, it can be seen clearly that charge accumulates directly below Li, and the corresponding accumulation lobe reflects the hexagonal symmetry of the graphite. Figs. 4.6(b-c) demonstrate the experimentally known fact, that a (2×2) monolayer is not a preferred construction for Li: Fig. 4.6(b) shows that charge is depleted between the Li atoms (blue color), and the electron localization function (ELF) [52] in Fig. 4.6(c) shows that there is no electron overlap between the Li atoms (blue color), i.e. the layer consists of separate adatoms, and it is not metallic. Corresponding visualizations of two K overlayers (Fig. 4.7) show that charge is depleted below the K slab and accumulated mostly above the C atoms of the topmost graphene layer (Fig. 4.7(a-b)), and in some extend between the K layers. The additional charge is transferred to the graphene π-bands (atomic p_z-orbitals), whereas depletion is observed in the sp^2 hybridized σ-bands of the topmost layer. From the electron density plot (not shown) it can be seen, that there is a sharp and flat boundary between the metal film and the "vacuum" which is in agreement with the He-scattering experiments [53].

Figs. 4.7(c-d) show that K forms a metallic layer (green color indicates a metallic bonding), and that there is no electron overlap in the adsorbate-substrate interface (blue region between the graphite and the metal layer). The blue rings around the individual K atoms correspond to the K $4s$ orbitals, and they indicate that the probability of finding two electrons within this range is negligible. The $3p$ semicore electrons
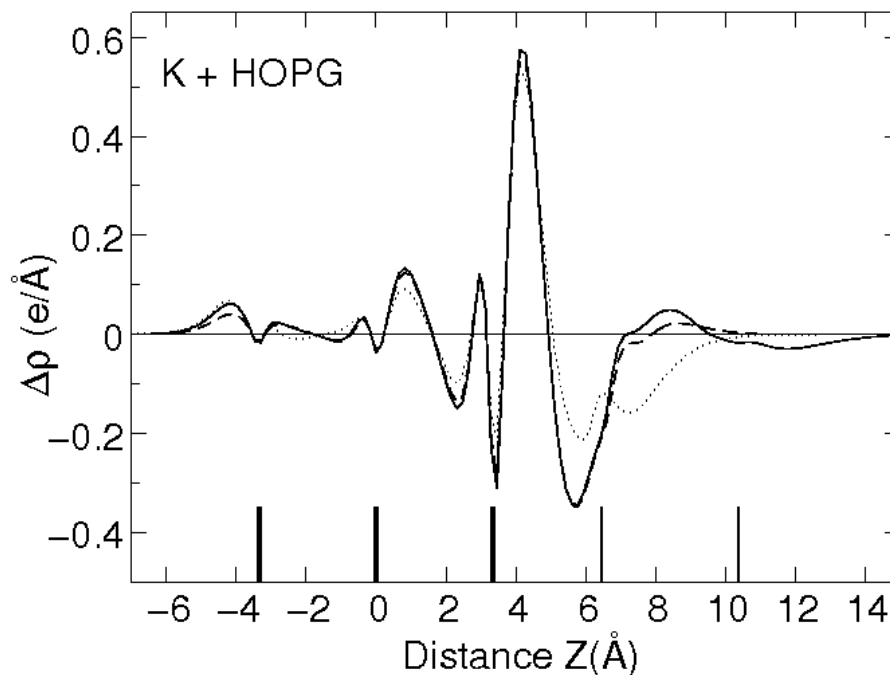
Figure 4.5: Laterally averaged charge density difference ($\Delta\rho_\perp$) of a K adatom (dotted curve), a (2×2) monolayer (dashed curve), and two (2×2) overlayers (solid curve) on graphite. The vertical bars denote the positions of graphene (thick bars) and K layers (thin bars). The charge densities have been calculated in an extended simulation box, so that the distance between the vertically repeated periodic graphite (GR) slabs is 20 Å.

that are included in the valence are mostly localized around the K atoms. A similar metallic behavior (delocalization of valence electrons within the metal layer) can be seen also in the corresponding figures of Rb and Cs MLs. This is expected as all the three largest alkali metals are found to form ordered (2×2) structures on graphite, and at least for K it is the most stable phase (monolayer).

ELF in Fig. 4.6 and Fig. 4.7 does not show any chemical bonding between the adsorbate and substrate as the interface region between them is blue (no electron overlap). This implies that the adsorbate-substrate interaction should be viewed as ionic in the alkali-HOPG systems.
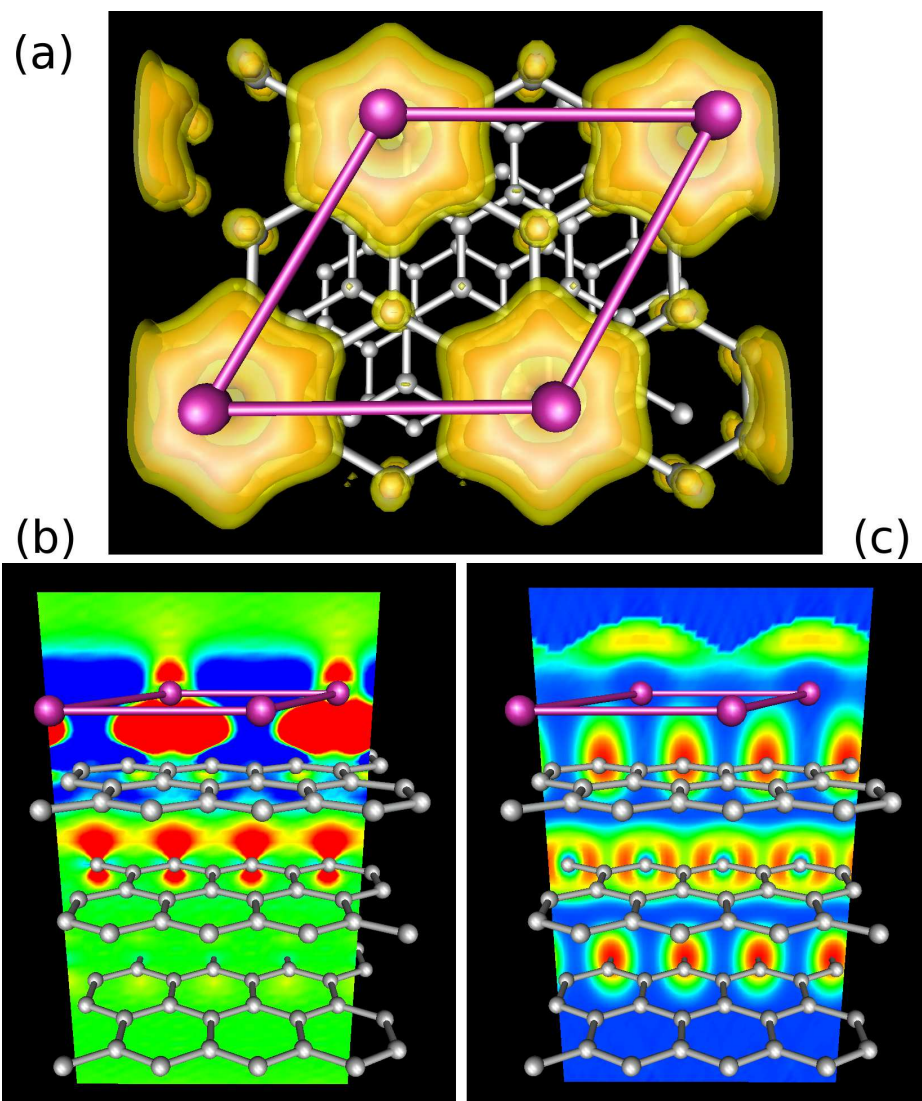
Figure 4.6: Visualization of the Li (2×2) monolayer on HOPG. (a) Three isosurfaces for the accumulated electron density. The corresponding values are 0.001 (yellow), 0.002 (orange), and $0.004e/\text{Å}^3$ (red), respectively. The Li atoms are marked by magenta spheres (b) Cutplane presentation of the charge density difference (xz plane), where the red color corresponds to accumulation ($0.0005e/\text{Å}^3$ or more) and blue depletion ($-0.0005e/\text{Å}^3$ or less). (c) The electron localization function (ELF, xz plane), where the red color corresponds to full localization (1.0, covalent bonds), green is analogous to homogeneous electron gas (0.5, metallic bonding), and blue equals to low localization (0.0).
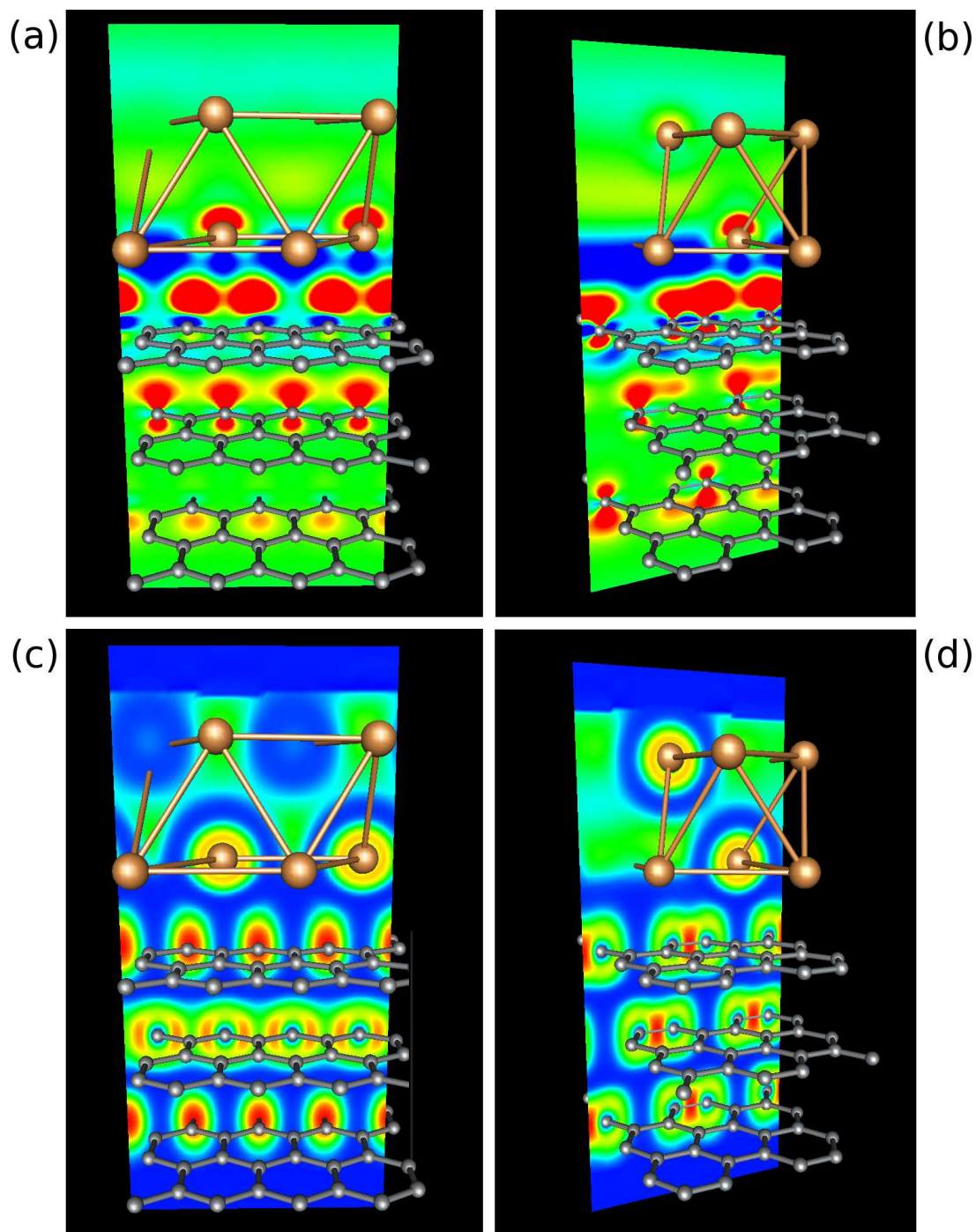
Figure 4.7: Cutplane visualization of two K (2×2) overlayers on HOPG. (a-b) The charge density difference is presented in xz and yz planes, where the red color corresponds to accumulation ($0.0005e/\text{Å}^3$ or more) and blue depletion ($-0.0005e/\text{Å}^3$ or less). (c-d) Similar presentation of the electron localization function (see the caption in Fig. 4.6).

4.3   Single-walled Carbon Nanotubes Inside Cyclic Supermolecules

In this section, the results of various pseudorotaxane systems consisting of carbon nan-otubes and crown ethers or β-cyclodextrin are discussed (article [III]). Three types of single-walled carbon nanotubes (SWNTs) have been considered: a metallic arm-chair (4,4) carbon nanotube (CNT(4,4)), a semiconducting zigzag (8,0) nanotube (CNT(8,0)), and a metallic zigzag (4,0) nanotube. Their diameters are 5.51, 6.36 and 3.38 Å, respectively. The first two SWNTs can be manufactured, whereas the existence of the third one is still questionable. In our calculations, the CNT(8,0) is threaded through a 36-crown-12 ether (CE-12) molecule, CNT(4,4) through 30-crown-10 ether (CE-10), and CNT(4,0) through β-cyclodextrin (β-CD), and the electronic proper-ties of the complexes are studied. These systems are named as CNT(8,0)@CE-12, CNT(4,4)@CE-10 and CNT(4,0)@β-CD, respectively. Furthermore, cross-linked ro-taxane systems are created by substituting four or two crown ether O atoms with N in the first two cases, and by abstracting two H atoms from the hydroxyl groups of β-CD.

The electronic structure calculations are performed with the Car-Parrinello molecular dynamics (CPMD) package [22]. Structural optimization is done with simulated an-nealing using the Car-Parrinello option for molecular dynamics as described in Section 2.4 (Γ-point calculation). Periodic boundary conditions are applied, and the electronic structure is calculated using 13 explicit **k**-points along the tube axis. The dimensions of the simulation box are chosen so that three to five nanotube unit cells are included in order to keep the periodically repeated macrocycles approximately 10 Å apart. The optimized box sizes along the tube axis are then 12.32 Å (80 C atoms), 12.82 Å (96 C atoms) and 16.82 Å (64 C atoms) for CNT(4,4), CNT(8,0) and CNT(4,0), respec-tively. To avoid interactions between the rotaxane complexes, the perpendicular box size is chosen so that the minimum distance between replicas is 8 Å or more.

The optimized geometries of the CNT(8,0)@CE-12 and CNT(4,4)@CE-10 complexes, and their cross-linked forms are shown in Fig. 4.8 (one replica included). The average C-O distance of 1.43 Å, and C-O-C angle of 111.5° are close to the corresponding gas-phase values of 1.43 Å and 111.8°. Small attraction between CNT(8,0) and CE-12 oxygens causes that the crown ether approaches the tube, which leads up to 20-30° change in the O-C-C-O torsional angles. The repulsive forces that are caused by the steric hindrance and strain are reflected in the considerable intermolecular C-O distances of 3.52 Å, but the total complexation energy is still slightly favorable (-0.12 eV). In the case of CNT(4,4)@CE-10 complex, the conformation is similar, but the smaller macrocycle diameter causes an additional strain in CE-10. This is observed as an elongated C-O bond length of 1.45 Å and a positive complexation energy of 1.16 eV. The intermolecular C-O distances of 2.86 Å are significantly shorter than
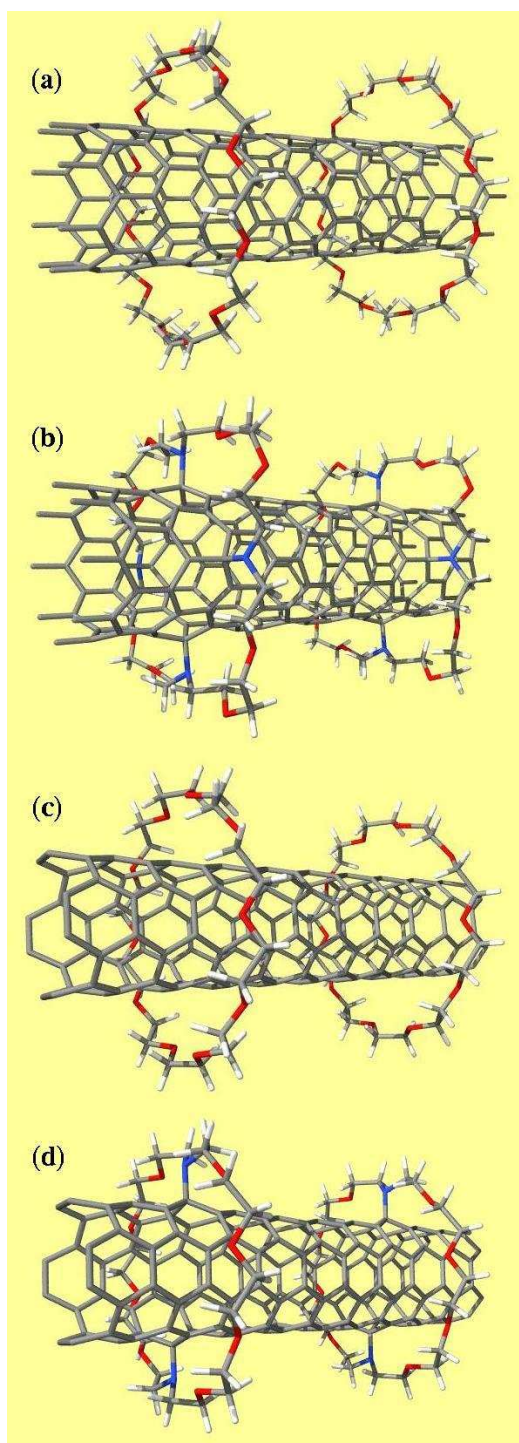
Figure 4.8: Geometries of CNT(8,0) and CNT(4,4) complexes before and after substitution of ether oxygens (red) with trifunctional nitrogens (blue). (a) CNT(8,0)@CE-12, (b) CNT(8,0)@CE-12N4, (c) CNT(4,4)@CE-10, and (d) CNT(4,4)@CE-10N2. The simulated systems are replicated once along the tube axis in order to show the separation of repeated macrocycles.

those of CNT(8,0)@CE-12. The cross-linking of CNT(8,0)@CE-12 by substituting symmetrically four O atoms with N leads to a considerable change in the system geometry (CNT(8,0)@CE-12N4). The covalent C-N bonds between the macromolecule and the tube force the macromolecule into a square shape, and the bonding of the corresponding C atoms changes from sp^2 to sp^3. The change in the bonding scheme can also be seen in the tube as elongated C-C distances of 1.52 Å (in pristine tube 1.42 Å), and the C-C-C angles of 103° and 112° are close to the tetrahedral value of 109.5°. A similar C-N bonding scheme can be seen for CNT(4,4)@CE-10N2 also.

The CNT(4,0)@β-CD complex is shown from two perspectives in the charge accumulation/depletion plot in Fig. 4.9. Macromolecule expands from its narrow end due to the steric hindrance effects with the tube, but the total complexation energy is only slightly positive (0.08 eV). The circular symmetric hydrogen bond network of the gas-phase conformation is partially broken, so that the separation of the polarized hydroxyl groups from the tube varies between 2.98 and 3.30 Å. There is no significant charge transfer between the tube and β-CD, and the interaction should be considered as polarization, as was the case with CNT(8,0)@CE-12 and CNT(4,4)@CE-10 systems. The charge accumulation/depletion profile is dominated by the covalent bond formation in the cross-linked cases. The cross-linked CNT(4,0)@β-CD complex is obtained via a hydrogen abstraction in two opposite hydroxyl groups, and the oxygens are forced to form covalent C-O bonds of 1.45 Å with the tube. Again, the hybridization of the affected CNT carbons changes from sp^2 to sp^3, and the tube diameter expands 0.5 Å in the vicinity of the contacts.
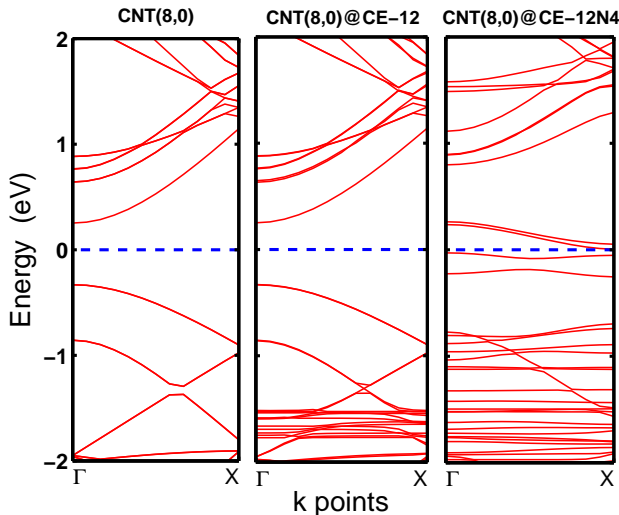
The electronic band structures of CNT(8,0) and its complexes with CE-12 and CE-12N4 are shown in Fig. 4.10. Simple analytical tight-binding calculations predict that an (8,0) zigzag tube is semiconducting [13], and our calculation result in a band gap of 0.5 eV at the Γ-point results from our calculations. Complexation with CE-12 does not perturb the band structure near the Fermi energy, and the only visible effects are the dispersionless bands below -1.5 eV corresponding to the HOMOs of the isolated CE-12. The band structure changes considerably when the system is cross-linked. The most important change is the appearance of four bands near the Fermi energy, which causes a peak in the corresponding DOS. The band gap has vanished, but there are no conduction channels available, and the system can be described as a semiconductor, despite the changes produced by the cross-linking.

Analytical considerations predict that the armchair CNT(4,4) tube is conducting [13]. This is confirmed by the electronic band structure (Fig. 4.11), showing a Fermi energy crossing (conduction band) near the Brilloun zone (BZ) boundary at the **X**-point, and the corresponding DOS has a finite weight. Our result is confirmed by the DFT study of Rubio et al. [54]. The band structure of CNT(4,4)@CE-10 complex is almost identical to that of CNT(4,4) despite the slight polarization caused by the artificially short intermolecular C-O distances. However, the cross-linking with CE-10N2 results
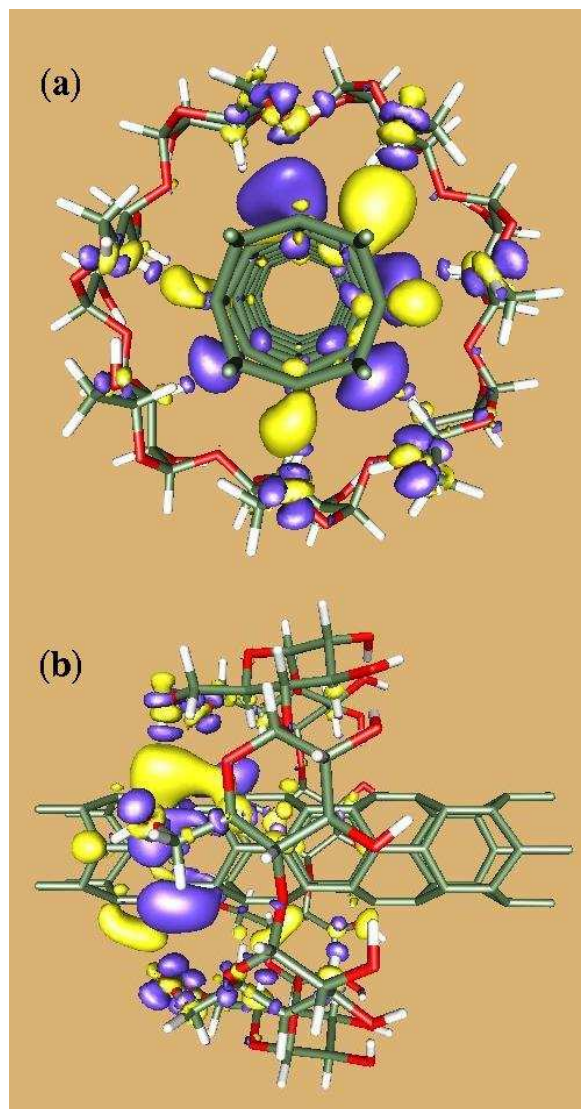
Figure 4.9: Charge accumulation/depletion plot of CNT(4,0)@γ-CD complex. (a) front view, (b) side view. The isosurface has a value of 0.00045 e/Å^3 both for accumulation (blue) and depletion (yellow).
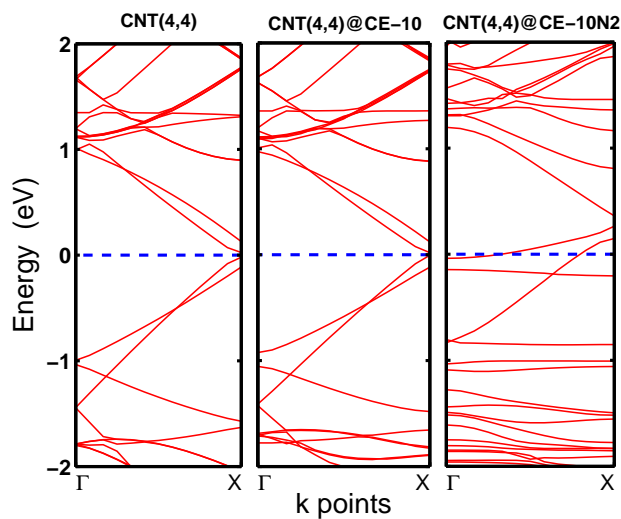
Figure 4.10: Electronic band structure of CNT(8,0) with and without CE-12 complexation (cross-linking). The dashed line at 0 eV corresponds to the Fermi energy. The simulation box includes three CNT(8,0) unit cells.

in significant changes in both the valence and conduction bands. In contrast to the pristine tube, there are bands of weak dispersion around the Fermi energy that give rise to a peak in DOS, and a new conduction channel opens enhancing the metallicity of the system.

In contrast to the analytical prediction for the zigzag tubes, the band structure of a small-diameter CNT(4,0) in Fig. 4.12 shows that the system is metallic with three conduction channels. The metallicity of SWNTs of diameters less than 5 Å has been observed in earlier studies [55], and it is suggested that this effect arises because of the severe tube curvature that causes a strong σ^*-π^* hybridization. Furthermore, it has been proposed that the tubes of diameter 4 Å or less should be superconducting [56]. However, a more detailed analysis by Ito *et al.* has shown that the main reason that CNT(4,0) is metallic is the strong C-C bond alternation (1.38 and 1.47 Å) that lowers (stabilizes) the first unoccupied π^*-band so that it crosses with the highest occupied π-bands [57]. We observe a similar phenomenon, and our values for the C-C bonds are 1.39 and 1.48 Å.

As with previous cases, a noncovalent complexation of CNT(4,0) with β-CD does not change the characteristic band structure of the nanotube, whereas the cross-linking with two hydroxyl oxygens has a clear effect. However, the cross-linking suppresses metallicity in this case as there are only two conduction channels available, and the DOS has a smaller weight at the Fermi energy. The probable reason is the elongation of the C-C bonds at the cross-linking sites (1.50-1.55 Å), which disturbs the symmetric bond alternation pattern that causes the metallicity of CNT(4,0).

Figure 4.11: Electronic band structure of CNT(4,4) with and without CE-10 complexation (cross-linking). The dashed line at 0 eV corresponds to the Fermi energy. The simulation box includes five CNT(4,4) unit cells.
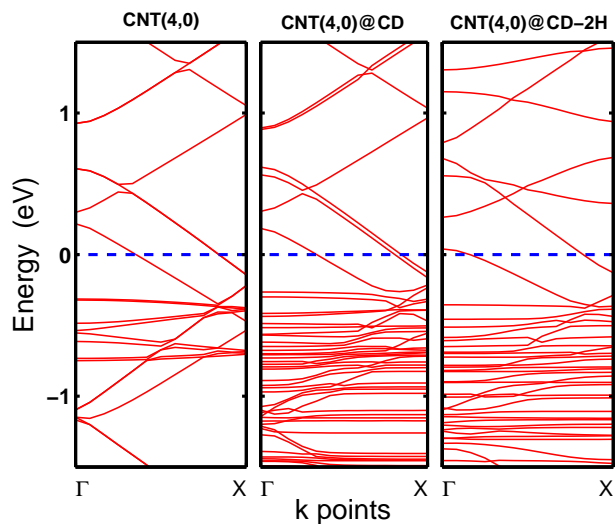
Figure 4.12: Electronic band structure of CNT(4,0) with and without β-CD complexation (cross-linking). The dashed line at 0 eV corresponds to the Fermi energy. The simulation box includes four CNT(4,0) unit cells.

5 Summary

This thesis consists of four separate articles and three different themes of research which involve nanometer-sized molecular constructions. The first study considers small magnesium clusters and their peculiar size-dependent insulator-to-metal transition. The second step was to study alkali metal adatoms, small alkali metal clusters and two-dimensional alkali metal monolayers on a graphite surface. This subject is covered in the second and fourth articles. The third topic is the one-dimensional pseudorotaxane complexes consisting of functionalized carbon nanotubes and cyclic macromolecules.

The ground-state geometries and electronic properties of Mg clusters in size-range Mg_2-Mg_{13} were studied using the first principles BO-LSD-MD simulation method [23], which uses the DFT based KS formalism, PBE parametrization of the exchance-correlation energy functional, separable and nonlocal pseudopotentials, and a plane wave basis set. This method is especially suited for studying isolated systems, such as free clusters. The dynamics in the finite-temperature simulation is handled with the BO approximation in conjunction with the classical Hellman-Feynman theorem of electrostatics. The study of small magnesium clusters showed that their metallization is slow and nonmonotonic, and it is not completed even for Mg_{13} which was the largest cluster size studied. Later studies have shown that metallization is not completed even for anionic Mg_{35} [36]. It was noticed that a reliable analysis of metallization has to be done using various indicators, not just one.

Carbon nanotubes and graphite are effectively infinite systems in one (tubes) or two (graphite surface) directions. The implemented periodic boundary conditions are the reason why Car-Parrinello molecular dynamics package (CPMD, [22]) was applied in their study. This first-principles method exploits the DFT based KS formalism as well in conjunction with separable nonlocal pseudopotentials, a plane wave basis set, and the PBE parametrization. The finite-temperature simulations were performed using the Car-Parrinello molecular dynamics in the case of pseudorotaxanes, and partially in the case of studying alkali metals on a graphite surface. Other geometry optimization schemes, such as the quasi-Newton approach (BFGS method [58]) or conjugate gradients were also applied in the optimization of the alkali metal-graphite systems.

The alkali metal atoms, clusters, and monolayers (Li, Na, K, Rb, Cs) on a graphite surface were studied, because their interaction with HOPG is still under debate [6]. It is found that after a certain coverage the alkali metals form metallic layers on

graphite which pronouncedly decouple from the surface. This can be seen as a drop in the adsorption energy, increase in the surface separation, and redistribution of the electron density. The electron localization functions of the system studied indicate that the adsorbate-substrate interaction is of ionic character. A single alkali metal atom has a considerable adsorption energy, and it prefers the hollow site on the hexagonal surface. The diffusion barriers are negligible, except for Li, and the alkali atoms are relatively mobile on HOPG. This explains partially the tendency of alkali metals to have several different phases depending on the coverage and temperature.

Both pristine and functionalized nanotubes are at the center of attraction in nanoscience. On the other hand, rotaxanes have been suggested as potential candidates for molecular devices or sensors in future nanotechnology. This is the reason to study polyrotaxanes consisting of small single-walled nanotubes and crown ether or β-cyclodextrin macromolecules. We found that the interaction of the circular macromolecules with CNT is weak, and they did not affect the electronic properties of the nanotube considerably. A cross-linking either by nitrogen substitution or hydrogen abstraction changes the pattern completely suggesting that it can be used for adjusting the CNT electronic properties. This could be exploited in nanocircuits and sensors, as cross-linked macromolecules could form specific binding sites for various chemical substances. Non-chemically bonded macromolecules could have an application in insulating nanotubes from each other, which could solve their bundling problem. Whether this kind of polyrotaxanes can be constructed in practice is still uncertain, but the first succesful experiments reported for self-organized CNT-polyrotaxanes are encouraging [59].

References

[I]   J. Akola, K. Rytkönen, and M. Manninen, *Metallic evolution of small magnesium clusters*, Eur. Phys. J. D **16**, 21-24 (2001).

[II]   K. Rytkönen, J. Akola, and M. Manninen, *Sodium atoms and clusters on graphite by density functional theory*, Phys. Rev. B **69**, 205404 (2004).

[III]   J. Akola, K. Rytkönen, and M. Manninen, *Electronic Properties of Single-Walled Carbon Nanotubes inside Cyclic Supermolecules*, J. Phys. Chem. B **110**, 5186 (2006).

[IV]   K. Rytkönen, J. Akola, and M. Manninen, *Density functional study of alkali atoms and monolayers on graphite (0001)*, Phys. Rev. B, submitted.

[1] W.D. Knight, K. Clemenger, W.A. de Heer, W.A. Saunders, M.Y. Chou, and M.L. Cohen, Phys. Rev. Lett. **52**, 2141 (1984).

[2] W.D. Knight, K. Clemenger, W.A. de Heer, W.A. Saunders, M.Y. Chou, and M.L. Cohen, Phys. Rev. Lett. **53**, 510(E) (1984).

[3] W. Ekardt, Phys. Rev. Lett. **52**, 1925 (1984).

[4] W. Ekardt, Phys. Rev. B **29**, 1558 (1984).

[5] A. Lyalin, I.A. Solov'yov, A.V. Solov'yov, and W. Greiner Phys. Rev. A **67**, 063203 (2003).

[6] M. Caragiu and S. Finberg J. Phys.: Condens. Matter **17**, R995 (2005).

[7] Z.H. Zhu, G.Q. Lu, F.Y. Wang, J. Phys. Chem. B **109**, 7923 (2005).

[8] T.W. Ebbesen, Phys. Today **49**, 26 (1996).

[9] S. Iijima, Physica B **323**, 1 (2002).

[10] M. Endo, *Mecanisme de croissance en phase vapeur de fibres de carbone (The growth mechanism of vapor-grown carbon fibers)*, PhD thesis, University of Orleans, France, 1975. (In French).

[11] H.W. Kroto, J.R. Heath, S.C. O'Brien, R.F. Curl, and R.E. Smalley, Nature (London) **318**, 162-163 (1985).

[12] S. Iijima, Nature (London) **354**, 56 (1991).

[13] R. Saito, G. Dresselhaus, M.S. Dresselhaus, *Physical Properties of Carbon Nanotubes* (Imperial College Press, Singapore, 2004).

[14] G.W. Gokel, W.M. Leevy, M.E. Weber, Chem. Rev. **104**, 2723 (2004).

[15] E.M.M. Valle, Process Biochemistry **39**, 1033 (2004).

[16] F.M. Raymo, J.F. Stoddardt, Chem. Rev. **99**, 1643 (1999).

[17] S.A. Nepogodiev, J.F. Stoddart, Chem. Rev. **98**, 1959 (1998).

[18] A. Szabo and N.S. Ostlund, *Modern Quantum Chemistry: Introduction to Advanced Electronic Structure Theory* (Dover Publications, New York, 1996).

[19] R.P. Feynman, Phys. Rev. **56**, 340 (1939).

[20] M. Weissbluth, *Atoms and Molecules* (Academic Press, New York, 1978).

[21] R.G. Parr and W. Yang, *Density-Functional Theory of Atoms and Molecules* (Oxford Univ. press, New York, 1989).

[22] D. Marx, J. Hutter, *Ab initio molecular dynamics: Theory and Implementation*, Modern Methods and Algorithms of Quantum Chemistry, J. Grotendorst (Ed.), John von Neumann Institute for Computing, Julich, NIC Series, Vol. 1, ISBN 3-00-005618-1, pp. 301-449, 2000.

[23] R.N. Barnett and U. Landman, Phys. Rev. D **48**, 2081 (1993).

[24] R. Car and M. Parrinello, Phys. Rev. Lett. **55**, 2471 (1985).

[25] CPMD V3.9 Copyright IBM Corp 1990-2005, Copyright MPI für Festkörperforschung Stuttgart 1997-2001.

[26] P. Hohenberg and W. Kohn, Phys. Rev. **136**, B864 (1964).

[27] W. Kohn and L. Sham, Phys. Rev. A **140**, A1133 (1965).

[28] M.P. Marder, *Condensed Matter Physics* (Wiley, New York, 2000).

[29] J.P. Perdew, K. Burke, and M. Ernzerhof, Phys. Rev. Lett. **77**, 3865 (1996).

[30] J.P. Perdew, *Electronic Structure of Solids '91*, (Akademie Verlag, Berlin, 1991), p. 11.

[31] W.E. Pickett, Comput. Phys. Rep. **9**, 115 (1989).

[32] C. Kittel, *Introduction to Solid State Physics* (Wiley, New York, 1996).

[33] N. Troullier and J.L. Martins, Phys. Rev. B **43**, 1993 (1991).

[34] D. Vanderbilt, Phys. Rev. B **41**, 7892 (1990).

[35] P. Pulay, Molec. Phys. **19**, 197 (1969).

[36] O.C. Thomas, W. Zheng, S. Xu, and K.H. Bowen Jr., Phys. Rev. Lett. **89**, 213403 (2002).

[37] J. Jellinek and P.H. Acioli, J. Phys. Chem. A **106**, 10919 (2002).

[38] P.H. Acioli and J. Jellinek, Phys. Rev. Lett. **89**, 213402 (2002).

[39] F. Reuse, S.N. Khanna, V. de Coulon, and J. Buttet, Phys. Rev. B **41**, 11743 (1990).

[40] V. Kumar, R. Car, Phys. Rev. B **44**, 8243 (1991).

[41] P. Delaly, P. Ballone, and J. Buttet, Phys. Rev. B **45**, 3838 (1992).

[42] M. Breitholtz, T. Kihlgren, S.-Å. Lindgren, and L. Waldén, Phys. Rev. B **66**, 153401 (2002).

[43] M. Breitholtz, T. Kihlgren, S.-Å. Lindgren, H. Olin, E. Wahlström, and L. Waldén, Phys. Rev. B **64**, 073301 (2001).

[44] N. Ferralis, K. Pussi, S.E. Finberg, J. Smerdon, M. Lindroos, R. McGrath, and R. Diehl, Phys. Rev. B **70**, 245407 (2004).

[45] F. Valencia, A.H. Romero, F.A. Ancilotto, and P.L. Silvestrelli, J. Phys. Chem. B **110**, 14832 (2006).

[46] Z.H. Zhu, and G.Q. Lu, Langmuir **20**, 10751 (2004).

[47] M. Khantha, N.A. Cordero, L.M. Molina, J.A. Alonso, and L.A. Girifalco, Phys. Rev. B **70**, 125422 (2004).

[48] M. Pivetta, F. Patthey, I. Barke, H. Hövel, B. Delley, and W.-D. Schneider, Phys. Rev. B **71**, 165430 (2005).

[49] L. Lou, L. Österlund, and B. Hellsing, J. Chem. Phys. **112**, 4788 (2000).

[50] D. Lamoen and B.N.J. Persson, J. Chem. Phys. **108**, 3332 (1998).

[51] F. Ancilotto and F. Toigo, Phys. Rev. B **47**, 13713 (1993).

[52] See, for example, A. Savin, R. Nesper, S. Wengert, and T.F. Fässler, Angew. Chem. Int. Ed. **36**, 1808 (1997).

[53] J.D. White, J. Cui, M. Strauss, R.D. Diehl, F. Ancilotto, and F. Toigo, Surf. Sci. **307-309**, 1134 (1994).

[54] A. Rubio, Y. Miyamoto, X. Blase, M.L. Cohen, S.G. Louie, Phys. Rev. B **53**, 4023 (1996).

[55] X. Blase, L.X. Benedict, E.L. Shirley, S.G. Louie, Phys. Rev. Lett. **72**, 1878 (1994).

[56] Z.K. Tang, L. Zhang, N. Wang, X.X. Zhang, G. H. Wen, G. D. Li, J. N. Wang, C. T. Chan, P. Sheng, Science **292**, 2462 (2001).

[57] A. Ito, Y. Natsume, S. Ohmori, K. Tanaka, Nano Lett. **2**, 629 (2002).

[58] R. Fletcher, *Practical methods of Optimization* (Wiley, New York, Vol. 1, 1980).

[59] H. Dodziuk, A. Ejchart, W. Anczewski, H. Ueda, E. Krinichnaya, G. Dolgonos, W. Kutner, Chem. Commun., 989 (2003).